

Growth Modes of Silver-doped Chalcogenide-based
Programmable Metallization Cells for Timing Applications

by

Amberly Ricks

A Thesis Presented in Partial Fulfillment
of the Requirements for the Degree
Master of Science

Approved April 2021 by the
Graduate Supervisory Committee:

Yago Gonzalez Velo, Co-Chair
Michael Kozicki, Co-Chair
Zachary Holman

ARIZONA STATE UNIVERSITY

May 2021

ABSTRACT

This research aims to investigate the material properties of various silver-doped germanium-chalcogenide thin films that novel lateral Programmable Metallization Cell (PMC) devices are based on. These devices are governed by a solid-state electrochemical reaction that is controlled electrically occurring at the micro and nanoscale.

By using various electrical and optical characterization techniques, useful material characteristics such as the activation energy of electrodeposit growth rate and bandgap energy can be extracted. These parameters allow for better tuning of these materials for more specific PMC device applications, such as a timer that can be placed into integrated circuits for metering and anticounterfeiting purposes.

The compositions of focus are silver-doped germanium-selenide and germanium-sulfide variations; overall, the bandgap energy of these materials decreases as silver content is increased, the activation energy tends to be smaller in sulfide-based devices, and chalcogenides highly doped with silver exhibit nanocluster migration growth modes due to the agglomeration of silver clusters in the film.

To Tata,

For teaching me that hard work can be fun.

ACKNOWLEDGMENTS

I would like to sincerely thank my advisors, Dr. Yago Gonzalez Velo and Prof. Michael N. Kozicki, for their unfailing support and guidance on my research, spanning most of my undergraduate and the entirety of my graduate career at Arizona State University (ASU). I would also like to thank my committee member, Prof. Zachary Holman, for his invaluable insight and willingness to help with my research throughout the years.

I would also like to thank my peers, who acted as mentors and as friends, Ninad Chamele, Smitha Swain, Priyanka Apsangi, Tal Sneh, Rajat Arora, and many others for their support and teamwork.

I am also very grateful for the staff at the ASU Eyring Materials Center, with special thanks to Diana Convey, Timothy Karcher, David Wright, and many others for their help and training.

TABLE OF CONTENTS

	Page
LIST OF TABLES	vi
LIST OF FIGURES.....	vii
CHAPTER	
1 INTRODUCTION	1
2 BACKGROUND	2
2.1 Programmable Metallization Cells	2
2.2 Chalcogenides	4
2.2.1 Chalcogenide Material Structure	4
2.2.2 Chalcogenide Photodoping	7
2.3 Device Mechanisms	10
2.3.1 Redox Reactions	11
2.3.2 PMC Growth Modes.....	15
2.4 Characterizations	18
2.4.1 Activation Energy	18
2.4.2 Bandgap Energy.....	20
3 MATERIALS AND METHODS	29
3.1 Fabrication	29
3.1.1 Thin Film Deposition	29
3.1.2 Cleanroom Processing	32
3.1.3 Mask Descriptions	32
3.1.4 Compositions Used.....	34

CHAPTER	Page
3.2 Growth	36
3.3 Characterization Methods.....	39
3.3.1 UV-Vis Spectrophotometry	39
3.3.2 Contact Stylus Profilometry.....	40
3.3.3 Optical Profilometry	42
3.3.4 Polarized Light Microscopy	43
4 RESULTS AND DISCUSSION.....	45
4.1 Study of Electrodeposit Growth.....	45
4.1.1 Electrodeposit Growth Rate Results.....	46
4.1.2 Electrodeposit Growth Rate Discussion.....	49
4.1.2.1 Channel Electric Field Effects	49
4.1.2.2 Electrolyte Composition Effects	54
4.1.2.3 Device Temperature Effects	58
4.2 Optical Characterization	64
4.2.1 Optical Characterization Results	64
4.2.2 Optical Characterization Discussion	65
4.3 Discussion.....	70
5 CONCLUSIONS	71
6 FUTURE WORK	73
REFERENCES	74
APPENDIX	
A GLOSSARY OF LATERAL PMC DEVICE MICROGRAPHS.....	78

B MEASURED THICKNESS VALUES OF DEPOSITED THIN FILMS.....83

LIST OF TABLES

Table	Page
1. Table 1	3
2. Table 2	7
3. Table 3	27
4. Table 4	30
5. Table 5	34
6. Table 6	35
7. Table 7	38
8. Table 8	45
9. Table 9	47
10. Table 10	48
11. Table 11	65

LIST OF FIGURES

Figure	Page
1. Figure 1.....	3
2. Figure 2.....	3
3. Figure 3.....	5
4. Figure 4.....	5
5. Figure 5.....	7
6. Figure 6.....	9
7. Figure 7.....	11
8. Figure 8.....	12
9. Figure 9.....	13
10. Figure 10.....	14
11. Figure 11.....	16
12. Figure 12.....	20
13. Figure 13.....	21
14. Figure 14.....	21
15. Figure 15.....	22
16. Figure 16.....	24
17. Figure 17.....	25
18. Figure 18.....	26
19. Figure 19.....	27
20. Figure 20.....	28
21. Figure 21.....	30

Figure	Page
22. Figure 22.....	30
23. Figure 23.....	30
24. Figure 24.....	31
25. Figure 25.....	33
26. Figure 26.....	34
27. Figure 27.....	36
28. Figure 28.....	37
29. Figure 29.....	38
30. Figure 30.....	40
31. Figure 31.....	40
32. Figure 32.....	41
33. Figure 33.....	41
34. Figure 34.....	42
35. Figure 35.....	43
36. Figure 36.....	44
37. Figure 37.....	44
38. Figure 38.....	44
39. Figure 39.....	50
40. Figure 40.....	50
41. Figure 41.....	52
42. Figure 42.....	53
43. Figure 43.....	58

	Figure	Page
44.	Figure 44.....	59
45.	Figure 45.....	59
46.	Figure 46.....	61
47.	Figure 47.....	62
48.	Figure 48.....	64
49.	Figure 49.....	69

CHAPTER 1

INTRODUCTION

As traditional electronic devices approach the limits of scalability, integrability, and cost, devices based on nanoionics have gained attention as the next generation in integrated circuits applications. Nanoionic devices have been introduced in non-volatile memory [1], [2], neuromorphic computing [3][1], and security applications including the timing devices in this research [4], [5]. This leads to the need to understand the underlying properties of the devices so they can be tuned to be best suited for the application. Because nanoionic devices rely on electrochemical sub-systems, the materials used and the transport of ions within them are a growing area of research.

This research will investigate the material properties these nanoionic devices are based on. Namely, germanium-based chalcogenide layers doped with silver act as the electrolyte in the timing devices. These timers have two electrodes on the electrolyte, constructed such that an electrodeposit forms between the two electrodes under bias; this electrodeposit growth has a time dependency with the applied bias [3]. This non-volatile growth can be used for metering and anticounterfeiting applications in which the bias-activated timer can be placed within an existing integrated circuit [4].

In using electrical and optical characterization techniques, important parameters from these devices, such as the activation energy of electrodeposit growth and the electrolyte's bandgap energy, can be extracted. These characteristics give insight to the underlying material structure and transport mechanisms occurring within the electrolyte and how they are affected by composition. Understanding the specifics of these materials allows them to be better integrated into new technologies.

CHAPTER 2

BACKGROUND

2.1 Programmable Metallization Cells

Programmable metallization cell (PMC) devices, also called electrochemical metallization (ECM) cells or conductive bridging random access memory (CBRAM) cells, exhibit a metal dissolution and metallization or electrodeposition through a solid-state electrochemical reaction [1]. Due to their high scalability and non-volatility, PMC devices are often referenced in a resistive switch-based array for memory applications [1], [2], [3]. The switching technology relies on electrically controlling the movement of metal cations to create an “ON” or “OFF” position [4]. Integrated circuit (IC) reliability and security is another field that lends itself to the use of PMC devices; a timing device can be fabricated by exploiting the time dependency of a changing capacitance resulting from specific PMC structures due to the controlled rate of electrodeposition [3], [4].

PMC devices are commonly structured in either a lateral or a vertical formation, where the ionic conductor, or the electrolytic layer, is sandwiched between metal layers or electrodes. Figure 1 shows a diagram of a vertical PMC structure used in a resistive-RAM (RRAM) cell [2][1]. Conversely, Figure 2 presents a diagram of a lateral PMC structure timing device [4]. In both structures, the electrodeposition occurs between the two electrodes, where one electrode acts as the “active” electrode, or the anode, and the other electrode acts as the “inert” electrode, or the cathode.

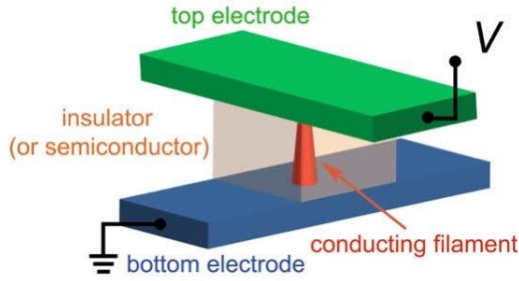


Figure 1: Cross-sectional diagram of a vertical PMC structure [1]



Figure 2: Cross-sectional diagram of a lateral PMC structure [4]

The choice of electrolyte used in PMC devices is limited due to the need for it to be electrically insulating and ionically conductive. Oxides and chalcogenides are the typical electrolytes used in PMC devices and tend to be paired with a silver or copper active electrode and a tungsten, platinum, or nickel inert electrode; Table 1 summarizes the compositions PMCs are based on from an academic survey [1].

Table 1: Summary of reported materials used in PMC devices [1]

Electrolyte	Active electrode (AE) metals	
	Ag	Cu
Ge_xS_y	W: [9, 87, 14, 49, 88, 48, 44, 95, 16]	W: [87]
Ge_xSe_y	W: [9, 49, 72, 50, 15, 43] Pt: [51] Ni: [49, 45, 94, 96]	W: [87]
Ge-Te	TiW: [90]	TaN: [38]
GST	Mo: [91]	
As-S	Au: [89]	
$\text{Zn}_x\text{Cd}_{1-x}\text{S}$	Pt: [39, 93]	
Cu_2S		Pt: [36, 46, 35] Ti: [41] ^a , [58] ^b Pt: [85, 36, 60] Ru: [86]
Ta_2O_5		W: [52, 92]; Pt: [36]; Ir: [36] W: [52, 82]
SiO_2	Co: [84]	
WO_3	W: [52]	
TiO_2	Pt: [81, 83]	
ZrO_2	Au: [98]	
MSQ ^a	Pt: [97, 32]	
GdOx		W: [52] ^c
$\text{Ge}_x\text{Se}_y/\text{SiO}_x$		Pt: [81]
$\text{Ge}_x\text{Se}_y/\text{Ta}_2\text{O}_5$		W: [52]
$\text{Cu}_x\text{S}/\text{Cu}_x\text{O}$		Pt: [81]
$\text{Cu}_x\text{S}/\text{SiO}_2$		Pt: [81]

^a Methylsilsesquioxane (transformed into SiO_2 upon annealing).

^b In these cases, the CE was a Ti/Pt/Au trilayer. The Ti may have been just a very thin 'sticking layer'.

^c In this case Cu-Te alloy was used as CE instead of pure Cu.

The PMC devices this research is focused on are germanium-based, silver-doped chalcogenides between a silver active-anode electrode and a nickel inert-cathode electrode. This combination is historically popular for PMC-related applications due to the high silver ion mobility within the doped chalcogenide layer [1].

2.2 Chalcogenides

Chalcogenides are materials that contain at least one element from the chalcogen group, which is group 16 on the periodic table (oxygen, sulfur, selenium, tellurium, and polonium). The chalcogens exhibit decreasing electronegativity and more metallic properties with increasing atomic number [6]. While oxides are often used in PMC applications (e.g. SiO_2), common chalcogenides refer to the other listed elements bonded with another electropositive element (e.g. GeS). In this research, germanium-based chalcogenides are used, where germanium is a common semiconductor with a bandgap energy of 0.66 eV. Germanium-based chalcogenides are preferred due to their ability to bond with the chalcogen atoms such as selenium and sulfur, host metals such as silver and copper, and due to germanium's thermal stability [7], [8].

2.2.1 Chalcogenide Material Structure

Thin films can be grouped into two categories: crystalline and non-crystalline. While crystalline materials are characterized by perfect, long range, periodic order, non-crystalline materials encompass matter which is not periodically ordered [10]. Figure 3 shows a simple schematic differentiating between a crystalline and non-crystalline structure.

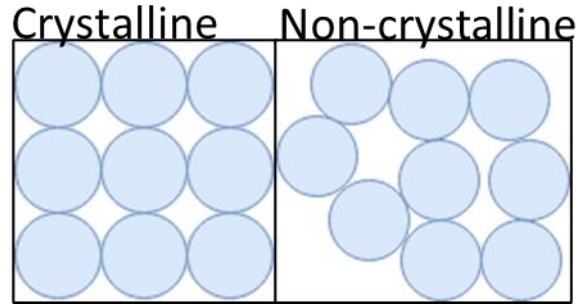


Figure 3: Schematic of crystalline versus non-crystalline order [10]

Glassy materials are often defined as materials which “can be solidified into a non-crystal from the melt” and is a subset of the amorphous, or non-crystalline, category [11]. Chalcogenides are often called “chalcogenide glass” due to their amorphous and insulating nature, in addition to their ability to form amorphous patterns from the melt [11]. Figure 4 outlines where chalcogenide glasses fall between the glass and semiconductor scales relative to other material groups and signifies that chalcogenide glasses exhibit semiconducting properties. Thus, these materials are characterizable by the material structure as well as the bandgap energy [10].

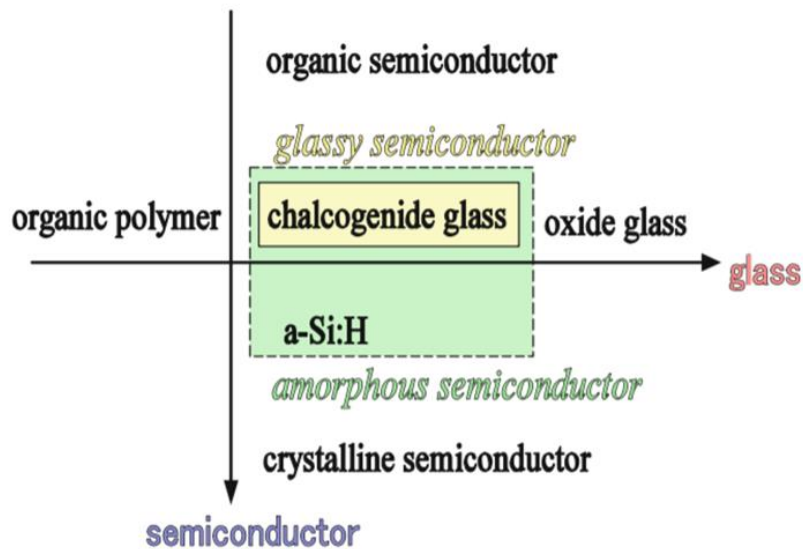


Figure 4: Characterizing glassy chalcogenides as a glass and semiconductor [11]

Chalcogenides are good contenders for PMC devices because when they are doped with silver or copper, they become ionic conductors [12]. This means that although the doped material still largely acts as an electric insulator, it allows the flow of ions. Of course, when the chalcogenide is doped, the material structure is changed. Silver is chosen as a dopant for these chalcogenides because it has a very high mobility and is a good electron supplier in the electrochemical reaction that must occur [9].

Because silver-doped germanium-based chalcogenides are the primary focus of this research, the structural changes in these specific materials are considered. Germanium-based chalcogenides (Ge-Ch) tend to display four structural elements, as confirmed by Raman spectroscopy experiments: Ge-Ch tetrahedra, Ge-Ge bonds, three Ch atoms connected to each Ge atom, and subsequent layering [9]. These structural elements occur in differing concentrations depending on how much germanium is present in the chalcogenide [9]. For example, as the percentage of germanium increases in a Ge-Ch composition, the number of tetrahedral units decrease and “chemical disorder” tends to increase due to the presence of Ge-Ge bonds [9]. This combination of structural elements leads to the presence of both “rigid covalent bonds mixed with soft van der Waals interconnections” in chalcogenide glasses [13]. Figure 5 displays how the structure in a germanium-sulfide chalcogenide is affected by increasing germanium content.

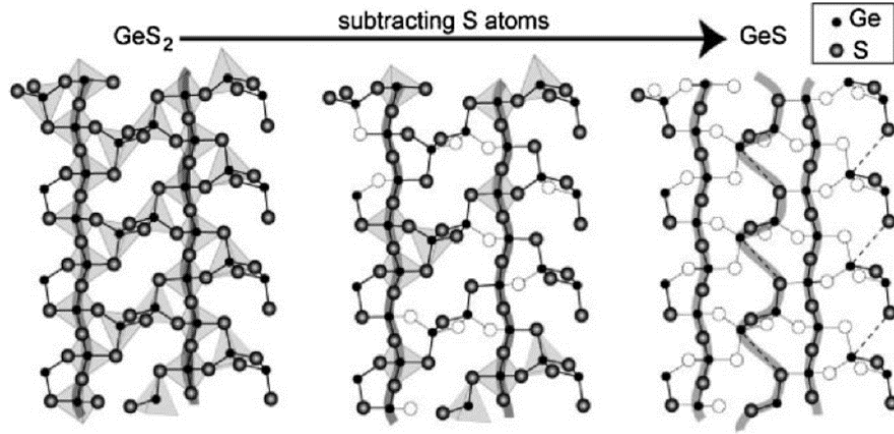


Figure 5: Structural development of increasing Ge atoms [9]

Of course, Ge-S and Ge-Se chalcogenides exhibit different bonding mechanisms, especially when a dopant such as silver is introduced. Research shows that Ge-S chalcogenides have a more relaxed structure than Ge-Se chalcogenides due to a low dimension of different bond clusters [13]. In addition, bulk GeS and GeSe compounds have the following electrical parameters at room temperature [14]:

Table 2: Summary of Ge-based chalcogenide bandgap and mobility values [14]

	Bandgap (eV)	Carrier Mobility (cm²V⁻¹s⁻¹)
<i>GeS</i>	1.18	529.57
<i>GeSe</i>	0.83	1045.40

Finally, generalized gradient approximation (GGA) functional calculations found GeS to have an indirect bandgap and GeSe to have a direct bandgap, supporting the smaller bandgap energy and larger carrier mobility values in GeSe bulk material [14].

2.2.2 Chalcogenide Photodoping

The structure is further affected by the addition of the silver dopant. Unique to glassy chalcogenides, silver dopants can be diffused into the chalcogenide layer at an

accelerated rate under light illumination [13]. This process, termed “photodiffusion”, occurs due to the movement of charged silver ions, electrons, and holes moving throughout the chalcogenide film [13]. More specifically, light incident on the chalcogenide glass forms charged defects which in turn creates an electric potential within the film when the light energy is above the optical bandgap energy of the chalcogenide [13].

When a thin film of silver is deposited directly on top of a thin film of chalcogenide, there is a finite “reacted” Ag-Ch layer. However, when the light is absorbed near this interface of reacted and unreacted layers, silver atoms can be ionized and become trapped by the defect holes created due to illumination [3], [13]. Because of the concentration of positive charges below the interface, electrons drive further into the chalcogenide; because of the resulting electric field from the positive silver ions and the electrons, the electropositive silver ions can overcome the potential barrier and drive further into the chalcogenide [3], [13]. This process is further ensured by the mix of structural elements present in chalcogenide glasses, which form channels ions can migrate through and be hosted [13]. Figure 6 shows a diagram of the photodiffusion process.

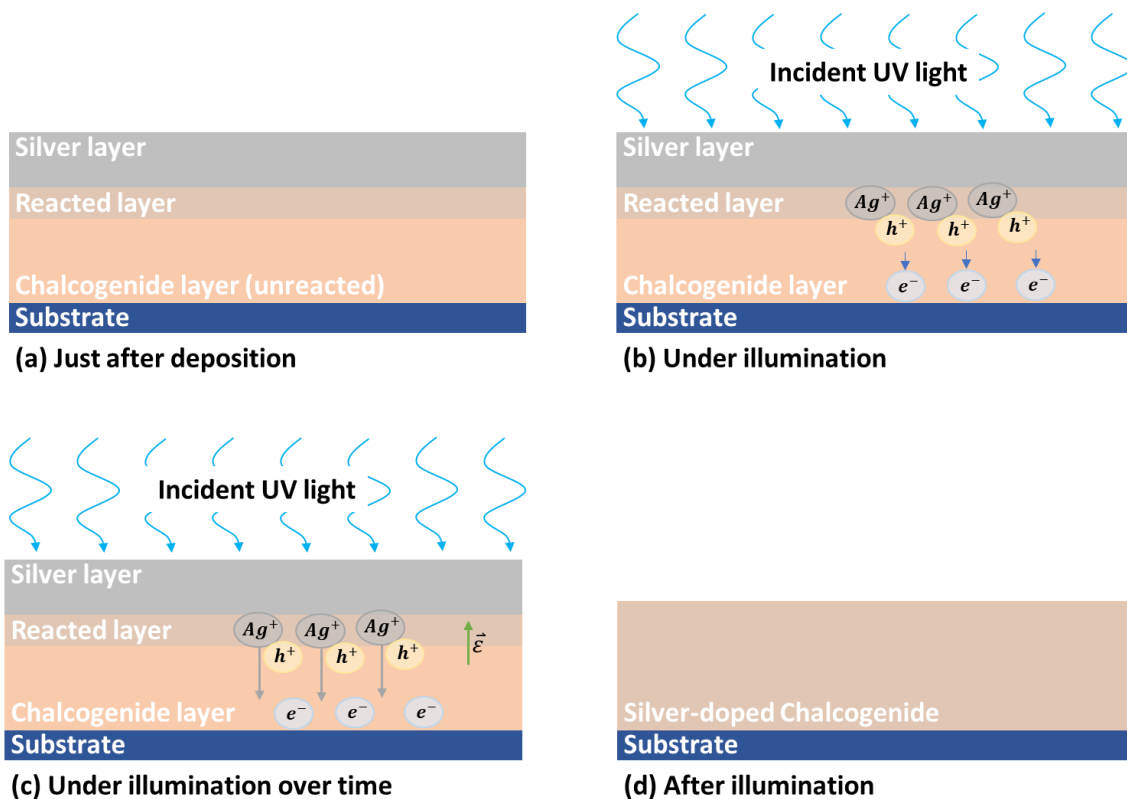


Figure 6: Cross-sectional diagram of photodiffusion process: (a) Silver and chalcogenide layers just after deposition with a thin reacted layer, (b) Under illumination, silver ions are positively charged and electrons interact at the reacted-unreacted interface, holes are driven into unreacted layer, (c) Under illumination, the silver ion-electron interactions create an electric field, silver ions are driven into the chalcogenide, (d) The silver photodiffuses into the chalcogenide to create a doped material layer

The photodiffusion process creates tertiary components within the electrolytic layer; it has been shown that silver-doped chalcogenides exhibit clusters of silver within the chalcogenide [13]. In germanium-sulfide (Ge-S) systems, Ag_2S and Ag_2GeS_3 nanocrystals are the products of photodiffusion and grow with increasing annealing temperature [13]. The main chalcogenide layer tends to become more “rigid and Ge-rich” after silver is photodiffused and much tetrahedral structure is lost [13]. For germanium-selenide (Ge-Se) systems, nanocrystals of Ag_2Se and Ag_8GeSe_6 result from photodiffusing silver. Unlike Ge-S systems, the nanocluster size depends on the “molar volume of the host” chalcogenide, where the host electrolyte becomes “Se poor” after

photodiffusion [13].

These structural changes resulting from increased germanium composition and silver photodoping are pertinent to understanding how these electrolytes aid in transporting ions in PMC device processes. For example, it is understood that silver-rich regions in the electrolyte that form silver “islands” (regions with a high concentration of silver-containing nanoclusters) are the main suppliers of silver ions, and groups of these nanoclusters can act as conducting pathways for ion transport [15]. These properties can be exploited to harness fast ion transport for PMC device use.

2.3 Device Mechanisms

Solid ion conductors tend to exhibit similar transport mechanisms, where ions are randomly thermally activated to hop from constrained site to constrained site [3]. Of course, inhomogeneities such as imperfect silver photodissolution or oxidation layers can lead to concentration gradients and phase separations within the electrolyte layer, which can affect ion transport [3][2]. In general, however, the ion hopping transport is catalyzed by drift and diffusion via charge concentration gradients and electric fields; this follows the trend of common ionic conductors, in which “ion current”, which is the flow of ions in the material, has an exponential relationship with applied electric field [3]. In other words, as the electric field present in the electrolyte is increased, the resulting ionic current experiences an exponential increase. This is especially pertinent in PMC devices, in which ion transport between electrodes directly impacts how quickly the resulting electrodeposit can grow.

Because the main aspect of PMC devices is the ability to control ionic current electrically, the electrochemical operation must be considered. The electrochemical system in a lateral PMC device is comprised of two electrodes on top of an electrolytic layer which acts as a channel. Figure 7 shows the electrodes and the electrolyte channel in the aforementioned lateral structure. Of the two electrodes, the active anode is composed of an oxidizable metal, such as silver or copper. The cathode is made of an inert metal, such as nickel, tungsten, or platinum [4]. The anode provides a source of cations while the cathode acts as cation sink [3]. The electrolytic channel is a chalcogenide thin film that is doped with the same metal as the anode, which allows for ease in cation transport. In this research, the electrolytic layer is a germanium-based chalcogenide doped with silver, the anode is silver, and the cathode is nickel.

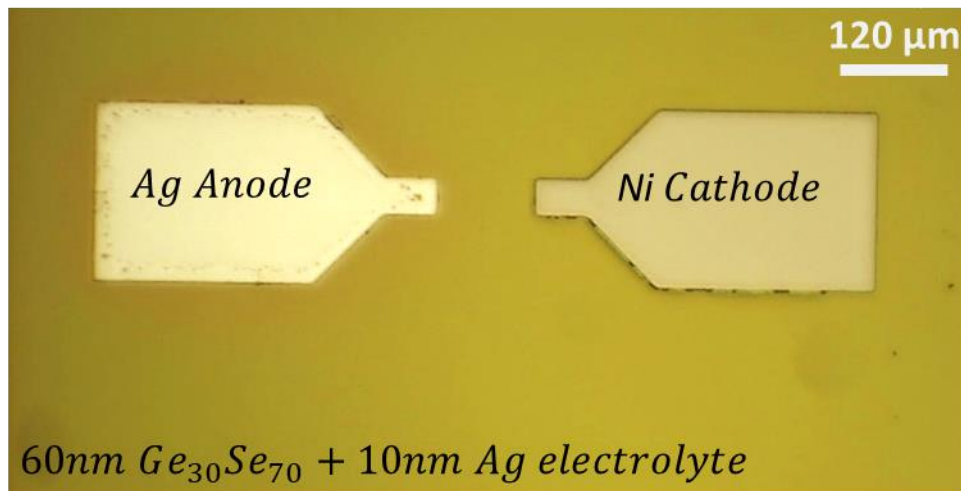
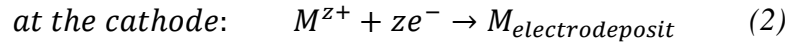
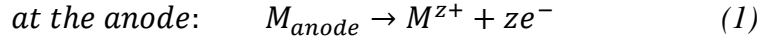


Figure 7: Top-view micrograph of 60 nm $\text{Ge}_{30}\text{Se}_{70}$ + 10 nm Ag chalcogenide lateral PMC device

2.3.1 Redox Reactions

In any electrochemical system, ionic current is only possible with a steady supply of ions and electrons. This relationship is known as a reduction-oxidation (redox) reaction and can be described by the following electrode half reactions [3]:



The electrons are supplied when a bias is applied between the two electrodes, as presented in Figure 8. Equation 1 shows that the metal in the anode is *oxidized* when the positive bias is applied, meaning the metal loses electrons; the oxidation half-reaction results in positively charged cations to exist freely in the electrolyte. Simultaneously, the reduction half-reaction, defined in Equation 2, occurs at the cathode, in which the free cations travel to and are *reduced* onto the inert cathode [3].

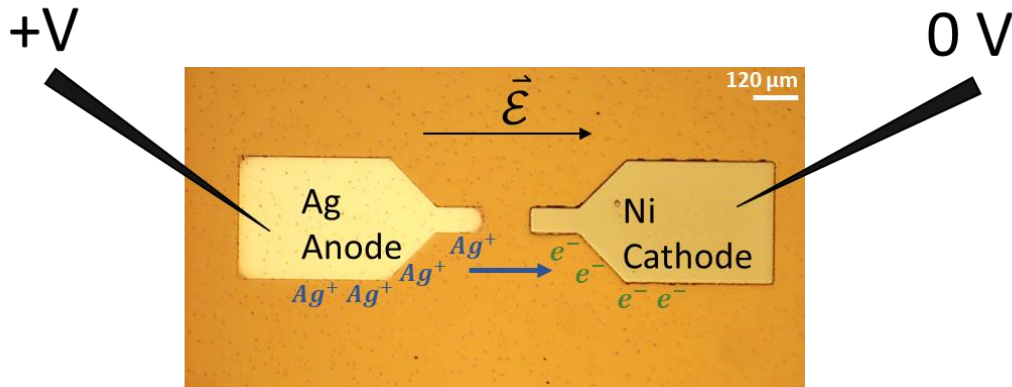


Figure 8: Bias and redox reaction diagram on 60 nm $\text{Ge}_{30}\text{Se}_{70}$ + 20 nm Ag chalcogenide PMC device

When the silver cations are reduced, they nucleate onto the inert cathode [16]. Nucleation is the process by which stable electrodeposit growth can occur through the initial formation of a stable nucleus [16]. After the cations complete the initial nucleation step on the cathode, successive silver cations will tend to nucleate on the ever-growing electrodeposit formation, and the electrodeposit “grows” in the opposite direction of the electric field back toward the anode. Figure 9 shows an example of the electrodeposit growth making a complete connection from the cathode to the anode.

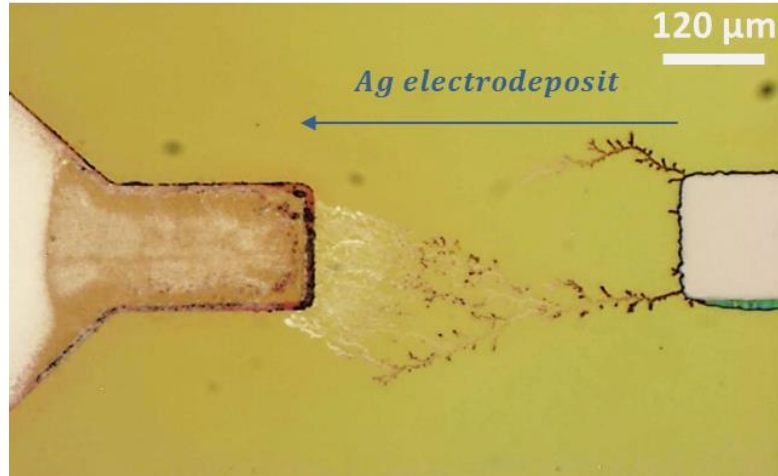


Figure 9: Ag electrodeposit growth diagram on 60 nm $\text{Ge}_{30}\text{Se}_{70}$ + 10 nm Ag chalcogenide PMC device

This electrodeposit growth continues until there is no longer a supply of electrons or ions—that is, until the bias is removed or the system is completely depleted of silver ions [16]. The choice of the inert cathode affects the rate of the redox reaction due to its potential of reducing into the chalcogenide and contributing to the redox reaction. This is why it is important that a sufficiently inert material is chosen, such that it does not dissolve into the electrolyte [1]. Further, because the silver ions nucleate onto the inert cathode during the reduction half-reaction, the cathode material can be chosen to either increase or decrease the overpotential needed to achieve nucleation. The initial nucleation is limited by the cathode material, and the effects are more present under low bias [3]. Therefore, the choice of the cathode material can be used to tune this added overpotential contribution from initial silver cation nucleation on the inert electrode.

As discussed before, the rate of ion transport in the ionic conductor is exponentially related to the electric field. In the case of these lateral PMC devices, the electrodeposit growth effectively reduces the width of the channel (the electrolyte region between the electrodes) as it gets closer to the anode. This reduction of channel width,

coupled with a constant bias between the electrodes, results in an increasing electric field over time within the channel, where Equation 3 gives a general approximation:

$$\vec{\varepsilon} = \frac{V}{d} \quad (3)$$

This increasing electric field increases the electrodeposition growth rate between electrodes and creates a phenomena in which the electrodeposit growth speeds up as it approaches the anode [3]. Figure 10 illustrates the changing effective channel width with electrodeposit growth.

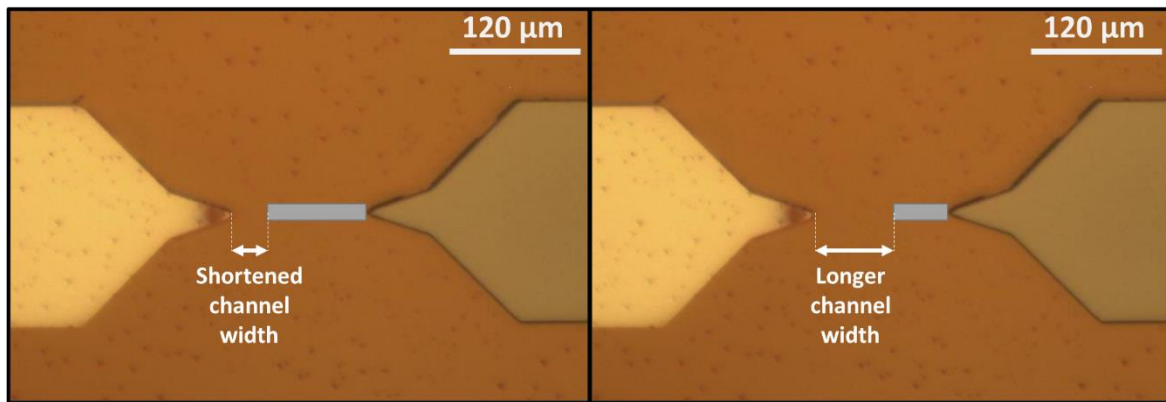


Figure 10: Effective channel width diagram on 60 nm $\text{Ge}_{30}\text{Se}_{70}$ + 20 nm Ag chalcogenide PMC device

It is clear that both electrolyte material structure and electrochemical processes affect ion transport behaviors. While both ion and electron availability must be in balance to have a successful redox reaction, material characteristics—and their influence on ion movement, such as with nanoclusters acting as conductive pathways—can also be described as limiting factors in ion transport behavior.

It is useful to consider ion mobility in this analysis, such that mobility is a measure of how quickly a carrier can travel in a material under the influence of an electric field, generally defined as:

$$\mu = \frac{v_d}{\varepsilon} \quad (4)$$

Redox rates, which measure how quickly the concentration of reactants in the reaction change with time, are also considered. Reaction rates are generally defined as:

$$rate = \frac{\Delta concentration}{\Delta time} \quad (5)$$

In this research, the $\Delta concentration$ refers to the concentration of silver cations and electrons, as described in the reaction Equations 1 and 2. Thus, ion mobility and redox rates are governing kinetic factors that describe electrodeposit growth [16].

2.3.2 PMC Growth Modes

Lateral PMC electrodeposit growth is grouped into four growth modes [16]:

1. High mobility, high redox rate
2. Low mobility, low redox rate
3. Low mobility, high redox rate
4. High mobility, low redox rate

Figure 11 summarizes these four growth modes, where Γ^j is the redox rate term.

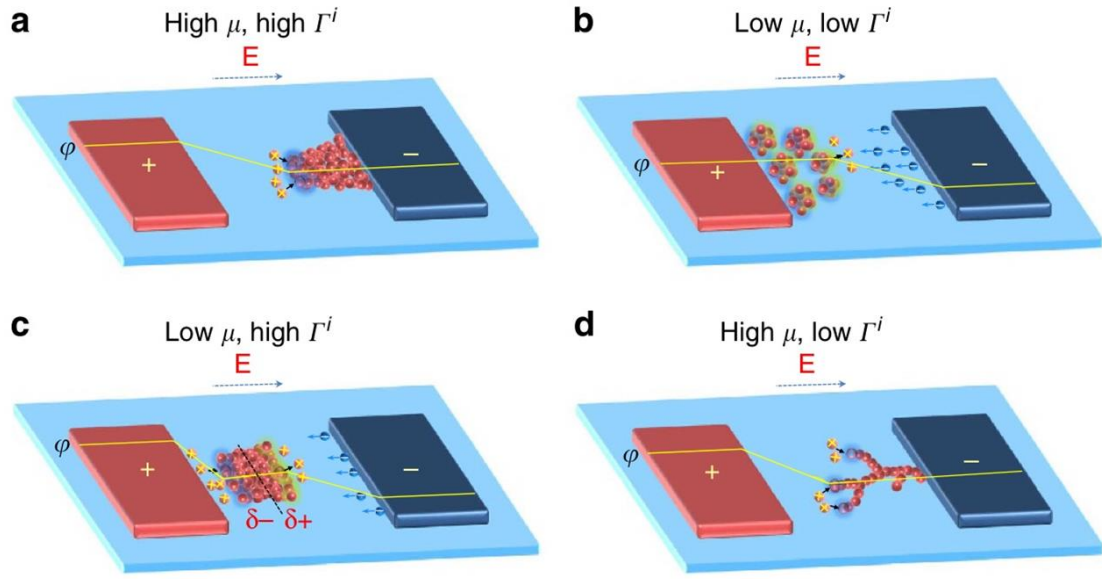


Figure 11: Qualitative model of filament growth modes governed by kinetic parameters mobility (μ) and redox rate (Γ^j): (a) Both μ and Γ^j are high resulting in electrodeposit growth from inert cathode to active anode, (b) Both μ and Γ^j are low resulting in nanocluster growth within the channel, (c) Low μ and high Γ^j resulting in electrodeposit growth within the channel, (d) High μ and low Γ^j resulting in branched electrodeposit growth from the inert cathode to the active anode [16]

In mode 1, cations nucleate at the cathode and grow from the cathode to the anode [16]. The large ion supply allows the growth to take on a dense, cone-shaped morphology. This corresponds to materials with high ionic conductivity because there is a large supply of ions that have high mobility in the electrolyte. The limiting factor in this mode is the reduction process, in which the depletion of ions in the system stops the reaction [17].

Mode 2 is characterized by ions nucleating inside the electrolytic channel and resulting in clustering [16]. Some reports have even shown the electrodeposit begins clustering near the active anode as a result of low ionic conductivity, and the ions nucleate on the clusters toward the cathode. The cation mobility is the main limiting factor in this mode, which is why the nanoclusters agglomerate [17].

Mode 3 growth is similar to mode 2 growth in that the ions tend to nucleate within the electrolytic channel, but due to high ion availability they tend not to nucleate in clusters but rather exhibit growth toward the cathode in a densely-packed filament [16]. This mode also has cation mobility as the limiting factor, as ion availability does not stop the cations from reducing within the channel [17].

Finally, growth mode 4 corresponds to ions nucleating on the cathode and growing toward the anode, but the limited ion supply leads to a branching effect [16]. The ions continue to reduce in high field-strength areas of the channel, as the cations prefer to reduce on the end of the existing filament [17]. This growth mode has also been observed in PMC structures with larger spacing between electrodes due to a smaller effective electric field leading to slower redox rates [17]. The main limiting factor in this growth mode is still cation mobility, posing an upper limit on cation concentration [17].

Overall, it appears that high ion mobility allows the cations to reach the inert cathode to reduce and nucleate there, whereas low ion mobility causes the cations to reduce and nucleate somewhere within the electrolytic channel. Further, high redox rates lead to denser electrodeposit growth due to high ion availability, and low redox rates cause clustering and branching effects [16].

Multiple modes can be observed simultaneously in a system as each stage of growth creates a new environment for further growth to continue [16]. In all, the ion mobility and redox rates can both act as limiting factors in the electrodeposit growth process as well as affect electrodeposit morphology. However, the cation transport process, and therefore cation mobility, seems to be the main limiting kinetic factor in most growth modes. This indicates that electrodeposit growth mechanisms are strongly

dependent on the choice of material composition since mobility is an inherent material property [17].

Further, temperature effects must be considered, as material properties—and therefore ion transport—tend to change with temperature. Both mobility and redox rates increase with an increase in temperature, which leads to a more mode 1-like growth regime [16]. The Butler-Volmer equation defines the current-voltage relationship in electrically-controlled ion-transfer processes at steady state [1]:

$$i = i_0 \left[\exp \left(\frac{(1 - \alpha)z_i e}{k_B T} \Delta\varphi_{charge} \right) - \exp \left(-\frac{\alpha z_i e}{k_B T} \Delta\varphi_{charge} \right) \right] \quad (6)$$

From Equation 6, the dependence on temperature is clear.

2.4 Characterizations

Chalcogenides can be characterized similarly to semiconductors; despite having glassy characteristics, the materials also have a bandgap energy comparable to common semiconductors [11]. Thus, electrical and optical characterizations of the chalcogenides yield important material parameters such as the activation energy of electrodeposit growth and the bandgap energy. These key figures give the ability to control and tune the electrolyte composition for specific PMC device applications.

2.4.1 Activation Energy

It is understood that while the PMC devices are controlled electrically, there are several mechanisms at play when it comes to electrodeposit growth. Thus, there exist events that have different Arrhenius behaviors within the material. The Arrhenius equation can be used to describe a relationship between the rate of some event and its

dependency on temperature, where K is the event, E_A is the activation energy, and T is the temperature at which the event took place:

$$K = Ae^{E_A/k_B T} \quad (7)$$

Generally, activation energy describes the energy required in a given system for a specified event to occur. This event can be the failure of a device, the completion of a reaction, or in this research, the growth of an electrodeposit in lateral PMC devices [28]. The activation energy of the electrodeposit growth rate is a good indicator of how much energy must be put in the PMC system to yield a complete electrodeposit growth—this energy is indicative of the transport mechanisms in the material [18].

Testing the electrodeposit growth rate as temperature is changed will provide data that exposes this Arrhenius dependency. In this research, the event is defined by the electrodeposit growth forming a connection from the cathode to the anode, and the time it takes for the growth to occur is the growth rate. Equation 8 can be reorganized as:

$$\ln(K) = \ln(A) - \left(\frac{E_A}{k_B}\right)\left(\frac{1}{T}\right) \quad (8)$$

By plotting $\ln(K)$ on the y-axis and $1/T$ on the x-axis, the resulting slope is $-E_A/k_B$, assuming the data indeed follows an Arrhenius behavior. Because k_B is simply the Boltzmann constant, the activation energy of the rate of electrodeposition is extracted. To create this plot, the time to short is measured and collected for a range of temperatures. Figure 12 shows an example of an Arrhenius plot:

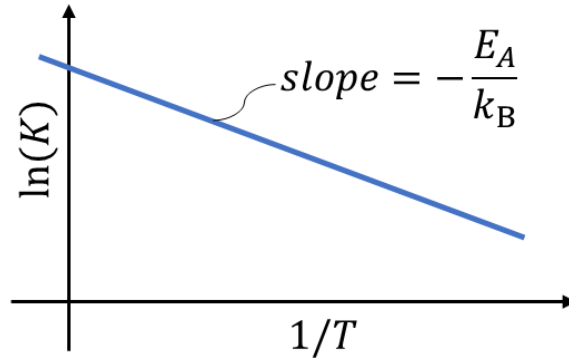


Figure 12: Example Arrhenius plot

2.4.2 Bandgap Energy

In order to extract the bandgap energy of the chalcogenide, other key parameters such as transmittance and absorption coefficient must be found first. Materials interact with light in three fundamental ways: transmittance (% T), reflectance (% R), and absorbance (% A). These three interactions sum up to one:

$$\%T + \%R + \%A = 100\% \quad (9)$$

Transparent materials allow light to transmit through, refracting at an angle due to the change in medium. Light can also be reflected and absorbed by a material, the latter in which the photon energy from light interacts with the material's electronic structure. Figure 13 demonstrates how the three interactions can result from incident light on a material.

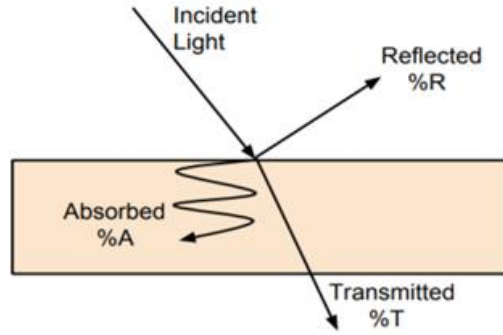


Figure 13: Transmittance, reflectance, and absorbance on a material [9]

Light absorbance in materials is an important aspect of characterizing materials because there are many phenomena occurring between the light and the matter. The *photoelectric effect* is a classical theory that posits: under certain conditions, if the energy of light incident on a clean surface is large enough, electrons will gain enough energy from the light photons to overcome their material workfunction and be emitted from the surface [20]. Figure 14 shows a simple diagram of the photoelectric effect.

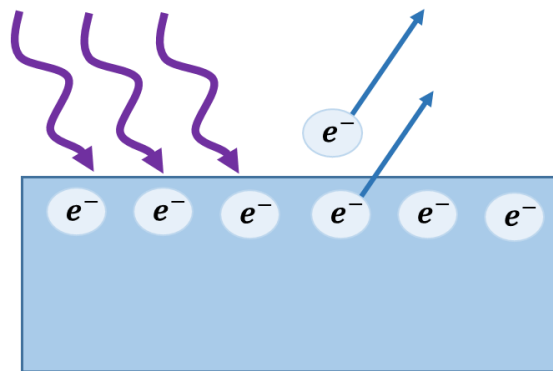


Figure 14: Simple diagram of light ejecting electrons from a material due to the photoelectric effect

The energy of the incident light is determined by the light wavelength, or frequency, where the relationship is:

$$E = \frac{hc}{\lambda} \quad (10)$$

The photoelectric effect is possible due to wave-particle duality, in which the momentum of a photon is given by:

$$p = \frac{h}{\lambda} \quad (11)$$

Because the light's frequency has an associated momentum related by Planck's constant, h , it is understood that light also behaves as a particle. In fact, electrons, and all matter, are governed by the wave-particle duality [20].

These physical processes are exploited for the purposes of transporting electrons for useful applications. Semiconductors are excellent materials for electron transport-based applications due to the ability to turn the electron transport “on” and “off”. Unlike metals, which contain free, conducting electrons, semiconductors have a finite energy “gap” between the valence band and the so-called conduction band. Figure 15 features an energy band diagram highlighting the bandgap energy, which is defined by the difference in energy between the conduction band and the valence band.

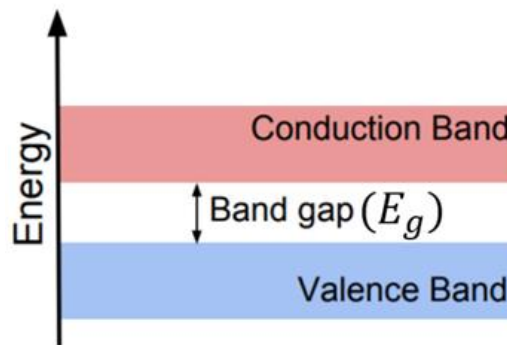


Figure 15: Energy diagram of the band gap in semiconducting materials [10]

Incident photons with an energy greater than the bandgap can be absorbed by the material and excite an electron to the conduction band. Electrons in the conduction band act like free electrons and can contribute to electron transport, or an electric current [20].

In understanding which wavelength of light, and therefore which photon energy, is absorbed by the material rather than transmitted or reflected, the optical bandgap energy can be deduced. Most of this photon absorption by semiconductors occurs in the ultraviolet and visible (UV-Vis) light range, so characterization and mathematical techniques will focus on this range.

The absorption coefficient is a material parameter that describes how far light can penetrate a material before it is completely absorbed by the material. It is dependent on material absorbance, and in liquid-state, can be described by the Beer-Lambert Law:

$$A = \epsilon bc = -\log\left(\frac{I}{I_0}\right) \rightarrow \alpha = \frac{2.303(A)}{t} \quad (12)$$

Small absorption coefficients indicate a material absorbs light poorly and will transmit the light if the material is thin, while larger absorption coefficients indicate a material will more readily absorb photons. There are various ways to calculate the absorption coefficient depending on the material structure, such as liquid-state, solid-state, or thin film. Because the thickness of a thin film is on the order of the wavelength of light in the UV-Vis range, light tends to reflect internally within the film—this occurrence requires that optical theory be taken into consideration when deriving the absorption coefficient for this research [22]. The derivation begins by first considering the spectral behavior or multiple internal reflections in a thin film [22]. Figure 16 shows a diagram of the light paths in a thin film, scaled by the reflection and absorption coefficients as it reflects internally:

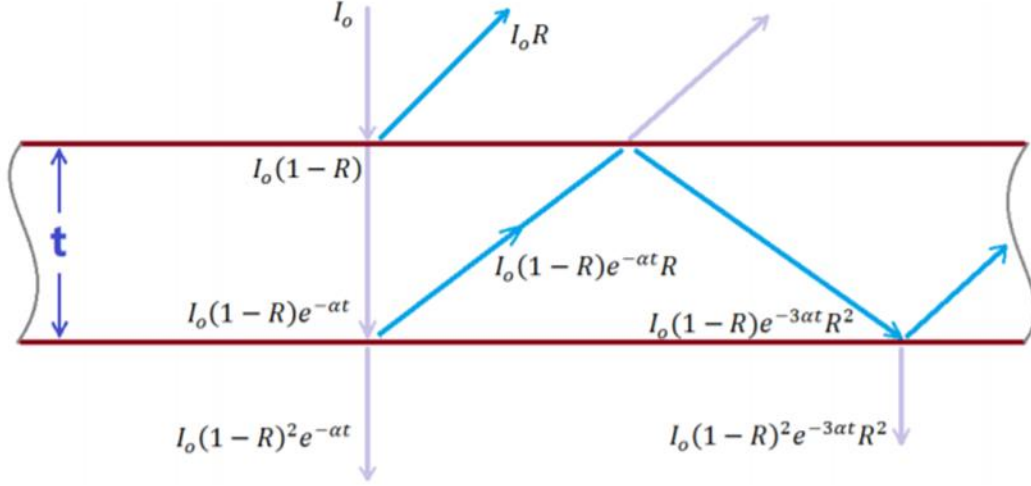


Figure 16: Intensity in multiple reflections in a thin film [22]

From Figure 16, the following series is defined for transmittance [22]:

$$\begin{aligned}
 T = \frac{I}{I_0} &= (1 - R)^2 e^{-\alpha t} + (1 - R) e^{-\alpha t} R \cdot R e^{-2\alpha t} (1 - R) \\
 &\quad + (1 - R) e^{-3\alpha t} R^3 \cdot R e^{-2\alpha t} (1 - R) + \dots \\
 &= (1 - R)^2 e^{-\alpha t} [1 + R^2 e^{-2\alpha t} + R^4 e^{-4\alpha t} + R^6 e^{-6\alpha t} + \dots] \\
 &= (1 - R)^2 e^{-\alpha t} [1 + R^2 e^{-2\alpha t} + (R^2 e^{-2\alpha t})^2 + (R^2 e^{-2\alpha t})^3 + \dots] \quad (13)
 \end{aligned}$$

The above geometric series is simplified:

$$T = \frac{(1 - R)^2 e^{-\alpha t}}{1 - R^2 e^{-2\alpha t}} \quad (14)$$

The absorption coefficient can then be derived for thin-film semiconductors [22]:

$$\begin{aligned}
 e^{-\alpha t} &= \frac{-(1 - R)^2 + \sqrt{(1 - R)^4 + 4T^2 R^2}}{2TR^2} \\
 &= \frac{1}{2R^2} \left[\sqrt{\frac{(1-R)^4}{T^2} + 4R^2} - \frac{(1-R)^2}{T} \right] \quad (15)
 \end{aligned}$$

Therefore:

$$\alpha = -\frac{1}{t} \ln \left\{ \frac{1}{2R^2} \left[\sqrt{\frac{(1-R)^4}{T^2} + 4R^2} - \frac{(1-R)^2}{T} \right] \right\} \quad (16)$$

In solid-state semiconductors, there are different modes of absorption. Figure 17 features the different regions of absorption, including (I) low energy, (II) absorption tail, (III) absorption edge, and (IV) high energy [22]. Electronic transitions occur above the absorption edge, so knowing what energy this region pertains to gives “information about the electronic states in the material” [23].

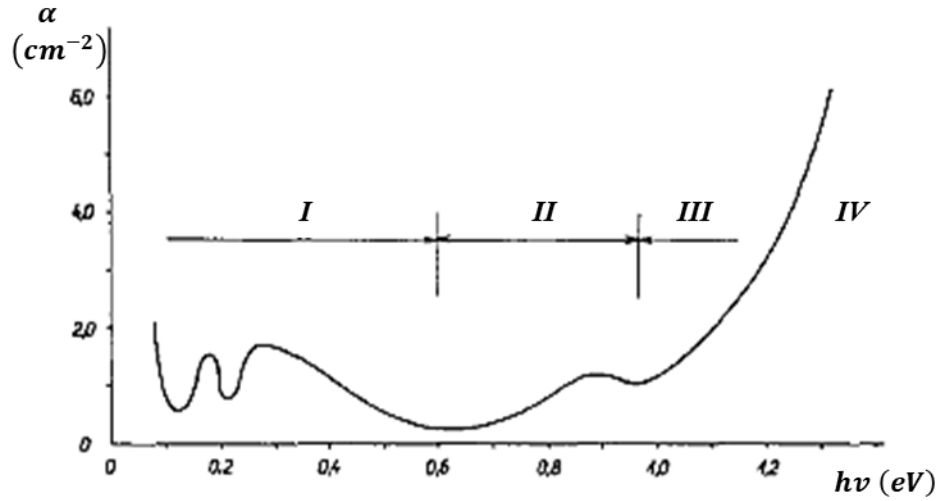


Figure 17: Absorption in amorphous germanium [23]

In the high absorption region, the absorption coefficient and the optical bandgap energy are related by the following Tauc relation [11]:

$$\alpha hv \propto (hv - E_g)^r \quad (17)$$

By measuring the transmittance of a chalcogenide thin film and calculating the absorption coefficient, the Tauc relation can be applied to extract the bandgap energy.

More specifically, the transmittance data is collected from 200 nm to 2500 nm in 1 nm

increments and reflectance is a calculated, singular value. The reflectance of these chalcogenide thin films only slightly varies over the measurement range, and so the R-value can be found using the following formula when $\alpha = 0$ [25]:

$$R = \frac{1 - T}{1 + T} \quad (18)$$

In equation 18, T is calculated from the average of the transmittance values over the transparent region in the resulting transmittance spectra [25]. This region is highlighted in Figure 18:

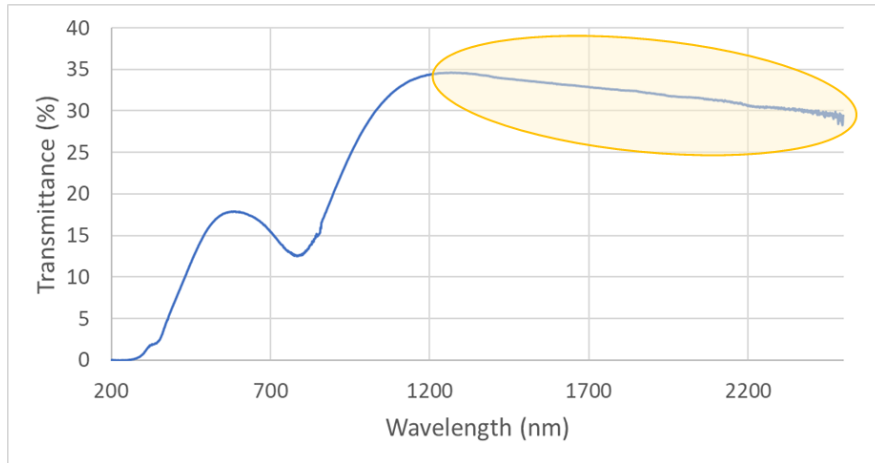


Figure 18: Transmittance spectra for 60nm $Ge_{40}S_{60}$ + 30nm Ag chalcogenide; transparent region highlighted where transmittance is high with respect to the rest of the spectra

After calculating the R-value, the absorption coefficient can then be found for each corresponding wavelength in the measured range. Past work measured the reflectance of the films for each wavelength corresponding to the transmittance data and used both of these values together to calculate the absorption coefficient [10]. Further research shows the Essick method, as demonstrated above, is more appropriate for R-value calculations for the chalcogenide films in this context [25].

By manipulating the data under Tauc's relation, Tauc plots can be plotted, in which the x-axis is energy, or $h\nu$, and the y-axis is $(ah\nu)^{1/r}$ [21], [23]. The r term in Tauc's relation determines which type of transition is occurring in the material's bandgap and is defined in Table 3 [24], and Figure 19 displays bandgap transition types in an energy-momentum diagram:

Table 3: Bandgap transition type and corresponding r values

$r = 1/2$	Direct allowed transition
$r = 3/2$	Direct forbidden transition
$r = 2$	Indirect allowed transition
$r = 3$	Indirect forbidden transition

- a) Direct allowed: requires absorption of photon
- b) Forbidden direct: requires absorption of photon, higher energy
- c) Indirect allowed: requires absorption of photon and phonon

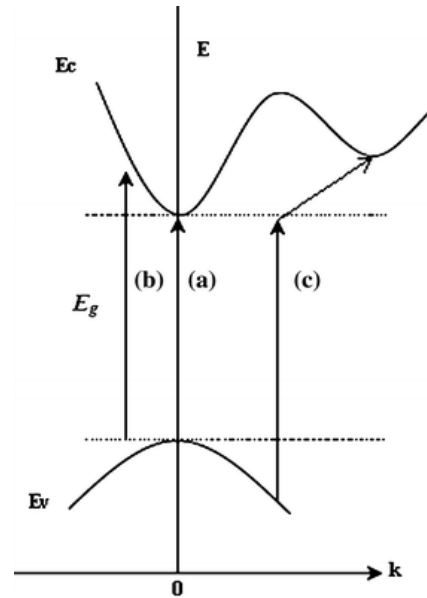


Figure 19: Bandgap transition types [24]

Studies show that $r = 1/2$ is acceptable for amorphous chalcogenide semiconductors including Ge-based chalcogenides [12], [26]. This research considers and tests all r -values, with $r = 1/2$ and $r = 2$ providing the best fits.

The resulting Tauc plot features a characteristic “knee” which represents the shift into the high absorption region. Extrapolating the linear portion of the plot to the x-axis yields the optical bandgap energy of the material [21], [24], [25]. Figure 20 shows a typical Tauc plot bandgap extrapolation:

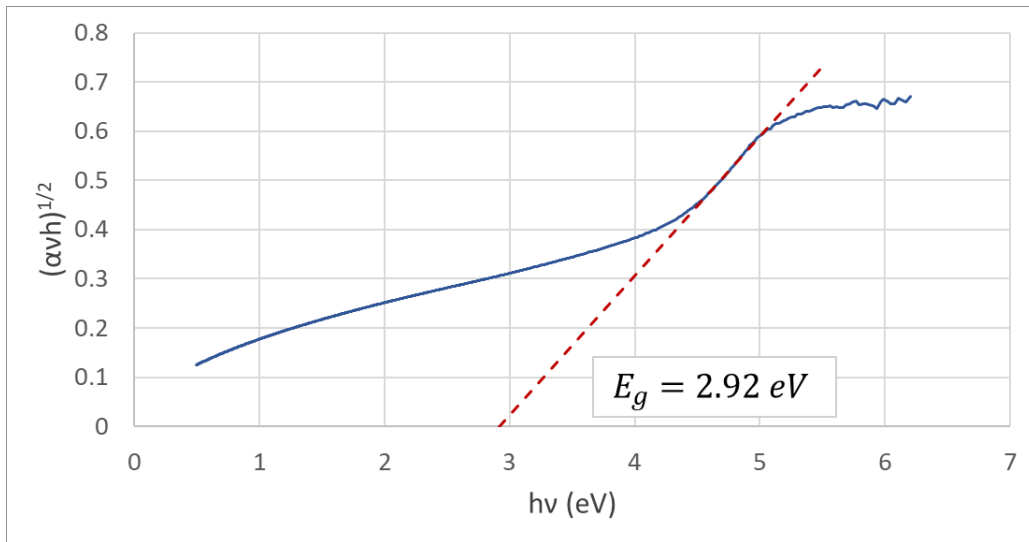


Figure 20: Tauc plot for 60nm $Ge_{40}S_{60}$ + 30nm Ag chalcogenide with extrapolated bandgap energy

CHAPTER 3

MATERIALS AND METHODS

3.1 Fabrication

Both PMC devices and thin film electrolytes were fabricated for this research. Thin film deposition was used for both sample types and the lateral PMC devices underwent further processing in the ASU NanoFab cleanroom.

3.1.1 Thin Film Deposition

The thin film layers of the electrolyte were deposited using physical vapor deposition (PVD). Specifically, a Cressington 308 Thermal Evaporation tool was used to coat the wafer with the chalcogenide and subsequent doping material of choice. Figure 21 shows a diagram of a thermal evaporating deposition system: the substrate is taped to the rotating stage at the top of the chamber and faces downward to the source. The source sits in tungsten resistive boats, shown in blue, that are connected to an external power supply. The deposition can take place at or below 10^{-6} mbar, at which point the heated source evaporates and coats the surface of the substrate. The Cressington 308 tool's stage rotates such that the substrate can be more evenly coated. Silver thin films are deposited directly on top of the chalcogenide film without breaking vacuum as both sources are contained within the chamber.

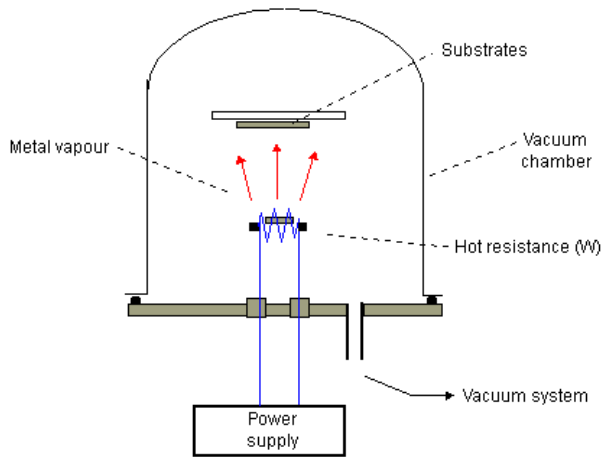


Figure 21: Cross-section diagram of a thermal evaporator deposition system [29]



Figure 22: Cressington 308 thermal evaporator

Table 4 outlines the average current values applied to each source material used in this research to maintain a 1 \AA/s deposition rate under vacuum. Figure 23 is an image of a heated resistive boat containing the silver source within the Cressington 308.

Table 4: Average applied current for different source materials

SOURCE MATERIAL	CURRENT (A)
Ge_xSe_{1-x}	22
Ge_xS_{1-x}	24
Ag	45



Figure 23: Hot resistive boat containing silver source shot

Thermal evaporation of thin films of electrolyte was used in both the first step of lateral PMC device fabrication and for other material characterization purposes. For lateral PMC devices, the doped chalcogenide was deposited onto a 4-inch Si wafer before going to the cleanroom for further fabrication processing. For optical characterization purposes such as UV-Vis spectrophotometry, the thin film electrolyte was deposited onto glass slides, as a transparent substrate is required [30]. Other characterization techniques could use unpatterned Si wafer pieces.

Silver-doping the chalcogenide is simply done by depositing a thin film of Ag directly on top of the thin film of chalcogenide without breaking vacuum. Once removed from the chamber, the samples were exposed to UV light for 30 minutes in order to diffuse the silver into the chalcogenide layer through photodoping. Figure 24 shows the UV light used to photodope the chalcogenide.

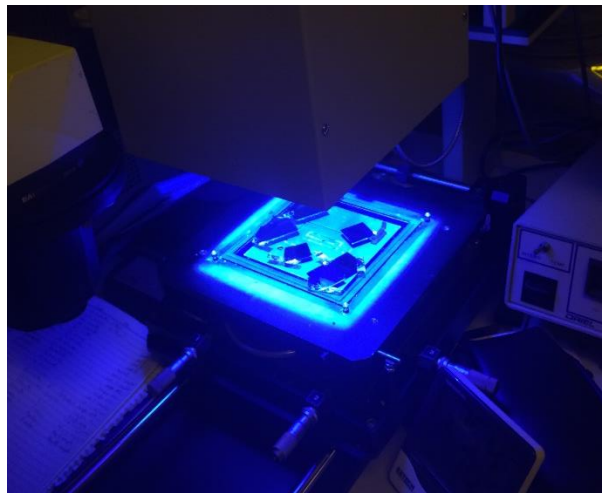


Figure 24: UV light incident on PMC device pieces freshly deposited with chalcogenide and silver layers to photodiffuse silver into the chalcogenide layer

Patterned samples that require Ag electrodes return to the Cressington 308 after being processed in the cleanroom to deposit 100 nm of Ag.

3.1.2 Cleanroom Processing

PMC devices consist of electrodes and layering that requires the use of the ASU NanoFab cleanroom. After the doped-chalcogenide layer is deposited onto the 4-inch Si wafer using the Cressington 308, it undergoes a photoresist masking process. Because the lateral PMC devices in this research consist of a 2-electrode lateral structure, the patterning process undergoes the following steps:

1. Mask 1 applied with AZ43300 photoresist spun at 2500 rpm
2. 100 nm nickel deposited to create inert electrode (cathode) using electron-beam evaporation
3. Mask 1 and nickel lift-off in acetone
4. Mask 2 applied with AZ43300 photoresist spun at 2500 rpm
5. 100 nm silver deposited to create active electrode (anode) using thermal evaporation
6. Mask 2 and silver lift-off in acetone

Step 5 utilizes the Cressington 308 tool to deposit the Ag electrodes, and the photoresist is removed using an acetone soak and a subsequent acetone-methanol-isopropanol (AMI) wash sequence.

3.1.3 Mask Descriptions

Because this research is focused on the time characteristics of electrodeposition growth between electrodes, and not capacitance, the lateral devices consist only of two electrodes and no bottom plate. The overall mask used to pattern the wafers is shown in Figure 25, where devices from the A and B groups were tested. Figure 26 highlights the device design of the A and B electrodes, where the A electrodes have a squared shape

and the B electrodes have a sharp shape. In both the A and B electrode designs, the electrodes are spaced 120 μm apart. It should be noted that the electrolyte can be patterned, which is depicted by the green rectangle that partially encompasses both electrodes; however, this research simply uses a blanket electrolyte over the entire wafer.

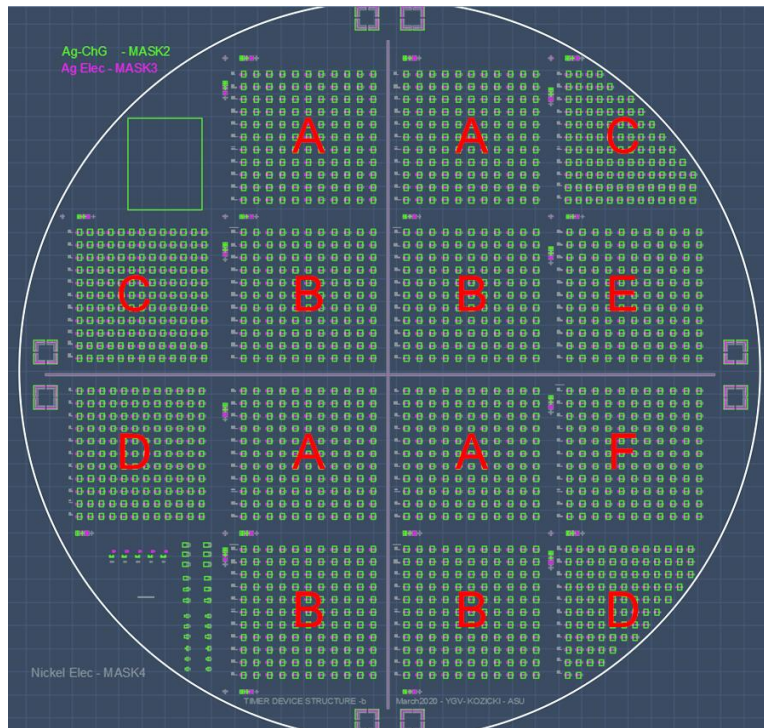


Figure 25: PMC mask layout with electrode design labels

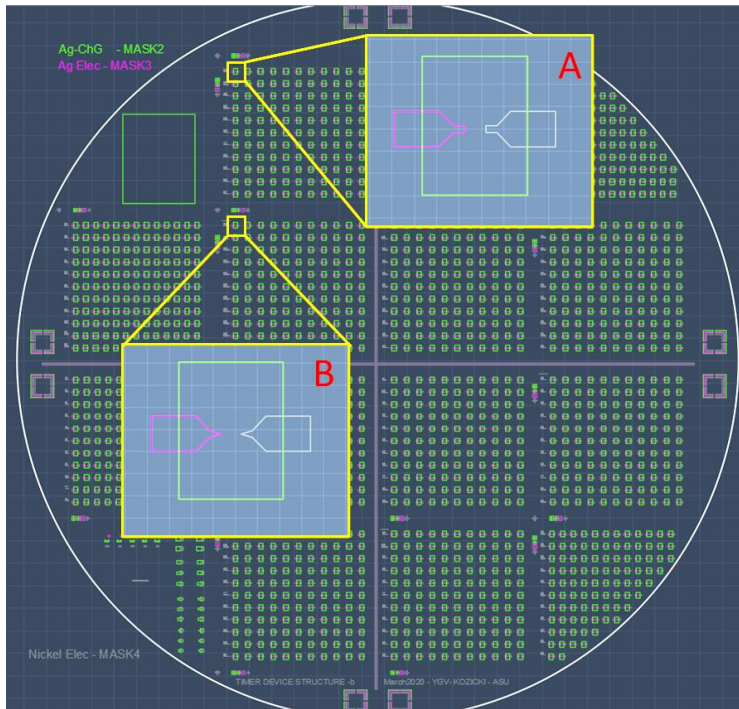


Figure 26: PMC mask layout with A and B electrode designs enlarged

3.1.4 Compositions Used

The following tables provide a comprehensive overview of the different compositions used in this research. Table 5 specifies the compositions of films deposited on lateral PMC devices used in growth and activation energy experiments, while Table 6 specifies the compositions of films deposited on 1mm quartz glass slides for UV-Vis spectrophotometry:

Table 5: PMC device electrolyte compositions

Chalcogenide	Doping	Photodoping
60 nm $Ge_{30}Se_{70}$	10 nm Ag	30 mins
60 nm $Ge_{30}Se_{70}$	20 nm Ag	30 mins
60 nm $Ge_{30}S_{70}$	10 nm Ag	30 mins

Table 6: UV-Vis spectrophotometry sample compositions

Chalcogenide	Doping	Photodoping	Radiation	Heating
<i>60nm Ge₃₀Se₇₀</i>	-	-	-	-
<i>60nm Ge₃₀Se₇₀</i>	<i>10nm Ag</i>	-	-	-
<i>60nm Ge₃₀Se₇₀</i>	<i>20nm Ag</i>	-	-	-
<i>60nm Ge₃₀Se₇₀</i>	<i>30nm Ag</i>	<i>30 mins</i>	-	-
<i>60nm Ge₃₀Se₇₀</i>	<i>30nm Ag</i>	<i>30 mins</i>	<i>1Mrad</i>	-
<i>60nm Ge₃₀Se₇₀</i>	<i>30nm Ag</i>	<i>30 mins</i>	-	<i>85°C</i>
<i>200nm Ge₃₀Se₇₀</i>	-	-	-	-
<i>200nm Ge₃₀Se₇₀</i>	<i>20nm Ag</i>	-	-	-
<i>60nm Ge₃₀S₇₀</i>	-	-	-	-
<i>60nm Ge₃₀S₇₀</i>	<i>10nm Ag</i>	-	-	-
<i>60nm Ge₃₀S₇₀</i>	<i>20nm Ag</i>	-	-	-
<i>60nm Ge₃₀S₇₀</i>	<i>30nm Ag</i>	-	-	-
<i>60nm Ge₄₀S₆₀</i>	<i>10nm Ag</i>	-	-	-
<i>60nm Ge₄₀S₆₀</i>	<i>30nm Ag</i>	-	-	-
<i>60nm Ge₄₀S₆₀</i>	<i>30nm Ag</i>	<i>30 mins</i>	-	-
<i>60nm Ge₄₀S₆₀</i>	<i>30nm Ag</i>	<i>30 mins</i>	<i>100krad</i>	-
<i>60nm Ge₄₀S₆₀</i>	<i>30nm Ag</i>	<i>30 mins</i>	<i>300krad</i>	-
<i>60nm Ge₄₀S₆₀</i>	<i>30nm Ag</i>	<i>30 mins</i>	<i>600krad</i>	-
<i>60nm Ge₄₀S₆₀</i>	<i>30nm Ag</i>	<i>30 mins</i>	<i>1Mrad</i>	-
<i>60nm Ge₄₀S₆₀</i>	<i>30nm Ag</i>	<i>30 mins</i>	-	<i>450°C</i>

The Ge₃₀Se₇₀ sample was heated to 85°C for 65 minutes, the Ge₄₀S₆₀ sample was heated to 450°C for 300 seconds.

3.2 Growth

To analyze the timing characteristics of these lateral PMC devices, the electrodeposit growth must take place. To “activate” the redox reaction on the lateral devices, a positive bias is applied to the active anode electrode and the inert cathode electrode is held at 0 V. This research evaluated the devices at a constant 2V bias and a constant 1V bias. Figure 27 shows a diagram of the experimental setup for electrodeposit growth, and Figure 28 features the probestation used in this research. To apply bias and monitor current, a Keithley 4200-SCS parameter analyzer was used. To control the probestation temperature, an INSTEC-mK2000 temperature controller was used.

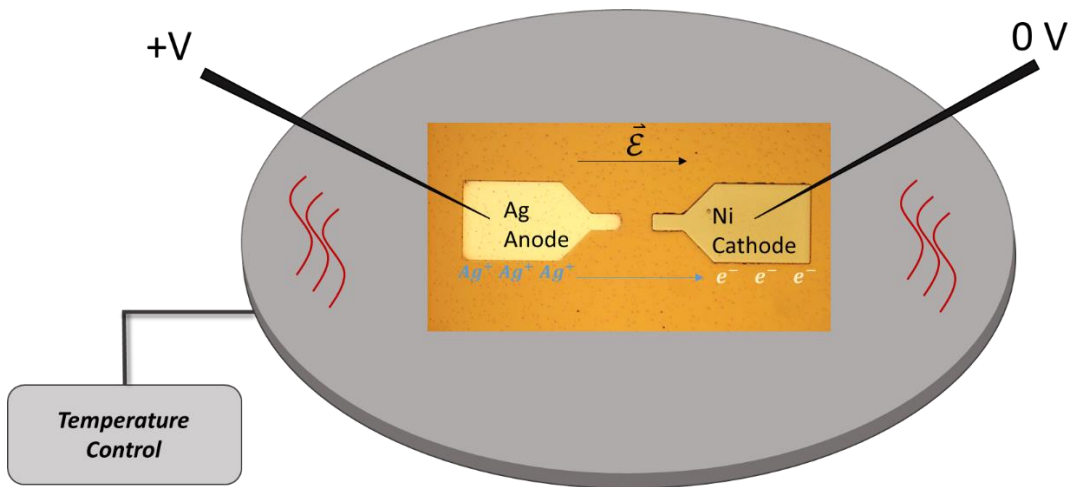


Figure 27: Electrodeposit growth experimental setup diagram

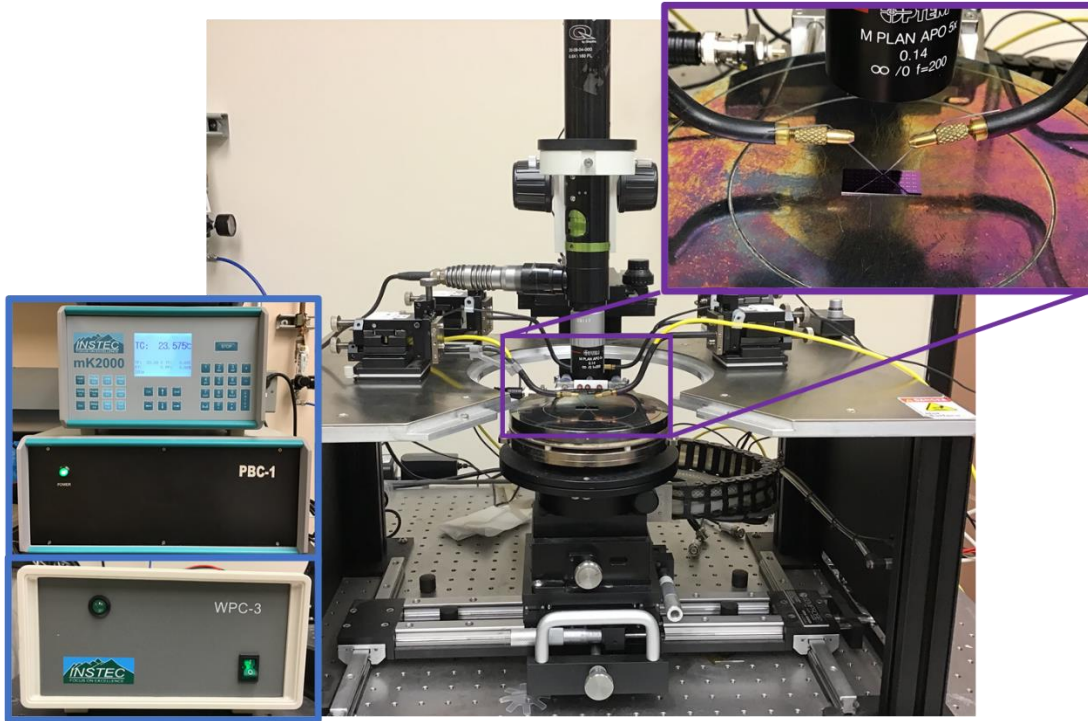


Figure 28: High temperature prober station, temperature control system (blue square), and probed PMC device (purple square)

The growth experiments took place on a high temperature prober station in order to evaluate the effects of device temperature on electrodeposition growth. Table 7 shows the temperatures used in growth experiments, starting from room temperature, and ending at 95°C. This upper limit was chosen because selenide-based chalcogenides experience a phase change near 80°C [31].

Table 7: Temperatures used in growth experiments

Temperatures
$T_1 = 20^\circ\text{C}$
$T_2 = 35^\circ\text{C}$
$T_3 = 50^\circ\text{C}$
$T_4 = 65^\circ\text{C}$
$T_5 = 80^\circ\text{C}$
$T_6 = 95^\circ\text{C}$

The experiments are conducted until the electrodeposit grows from the cathode to the anode and forms a connection. This connection is clearly observed in current-time plots when the current spikes from its low state to its high state. Figure 29 shows an example of a typical current-time curve, where the red arrow denotes the instant in which the electrodeposit forms a connection between the electrodes.

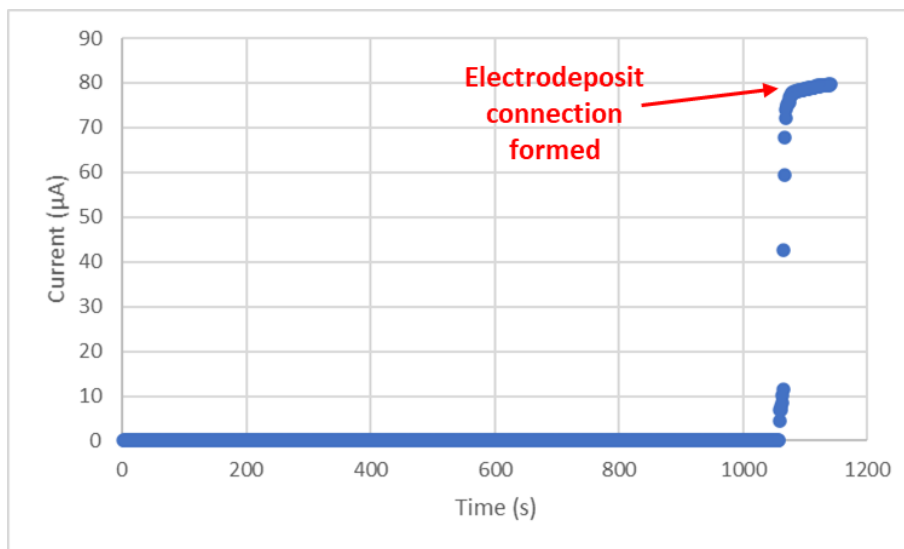


Figure 29: Current-time plot from a 60 nm $\text{Ge}_{30}\text{Se}_{70}$ + 10 nm Ag PMC device with square electrodes grown at constant 2 V

3.3 Characterization Methods

Optical, electrical, and physical characterization techniques were used in this research to better understand the properties of the materials used in the PMC devices.

3.3.1 UV-Vis Spectrophotometry

UV-Vis spectrophotometry is an optical characterization technique that utilizes light in the ultraviolet and visible spectra to analyze optical characteristics of a material. This method produces transmission data that is later analyzed to find the absorption coefficient and optical bandgap energy, as derived before. The Perkin Lambda 950 was used in this research and uses simple optics to measure this data; it contains two lamps, a series of mirrors, and diffraction gratings used to direct and separate wavelengths of light to the sample. Figure 30 shows a diagram of a UV-Vis spectrophotometer, and Figure 31 shows the analogous inside of the Perkin Lambda 950. The sample is placed in front (location A) of the integrating sphere, a nearly 100% reflecting chamber, to measure transmission; all the wavelengths that pass through the sample are collected in the integrating sphere (blue arrows) and compared to a reference light (purple arrows). The Perkin Lambda 950 has a wavelength range of 175 nm – 3300 nm, and this research uses a wavelength range of 200 nm-2500 nm.

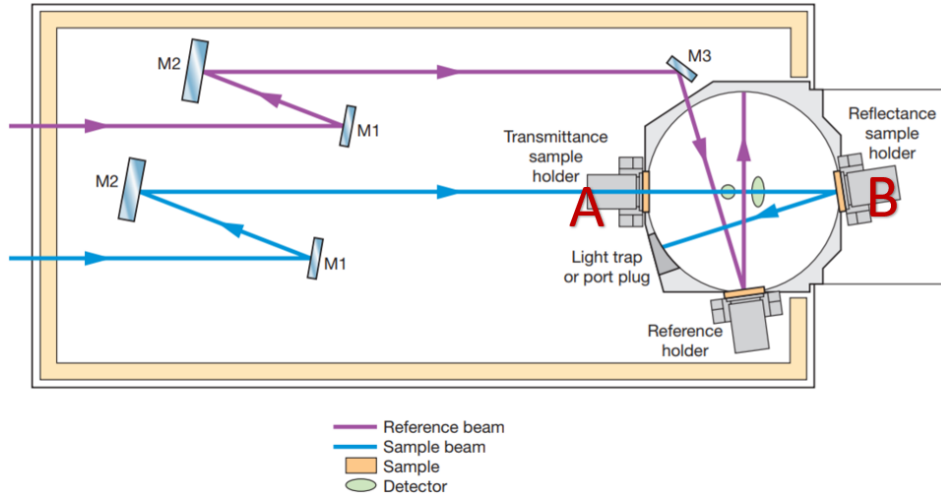


Figure 30: Diagram of UV-Vis spectrophotometer light paths [10]



Figure 31: Top view of open Perkin Lambda 950 UV-Vis spectrophotometer [10]

3.3.2 Contact Stylus Profilometry

Contact stylus profilometry is used to measure vertical variations from about 1 nm to 1 mm in a film. Using a diamond-tip, the stylus moves across a portion of the film's surface linearly and detects vertical changes. The Bruker Dektak XT Stylus Profilometer

models hills and valleys which is useful for accurately measuring the thickness of a film or device feature. A diagram of how the stylus moves is shown in Figure 32, and the Bruker Dektak profilometer used in this research is shown in Figure 33. It is important to note that the stylus can scratch the film, so this characterization technique is performed after other characterization methods. This research utilized the stylus profilometer to measure the thickness of deposited thin films and electrodes as well as to gauge surface roughness.

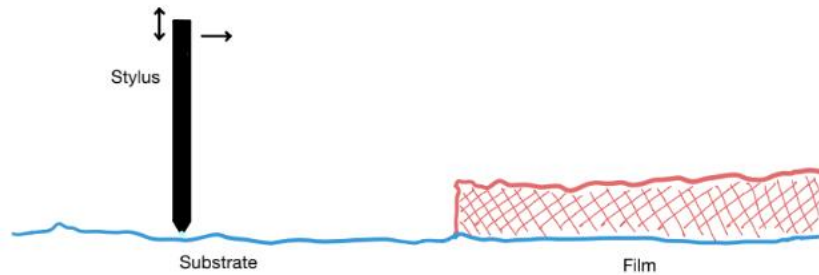


Figure 32: Cross-sectional diagram of stylus moving over a thin film [10]

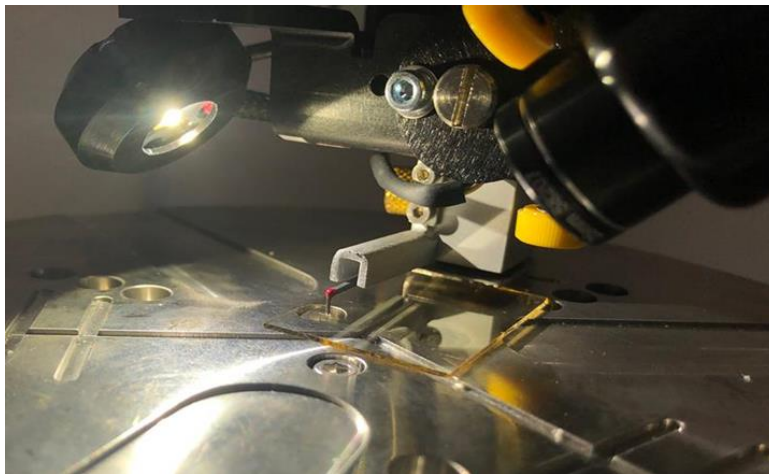


Figure 33: Bruker Dektak XT Stylus Profilometer needle on a chalcogenide thin film [10]

3.3.3 Optical Profilometry

Optical profilometry is another optical characterization technique that is used to evaluate the topography of the surface of a sample. This research used the Zygo ZeScope Optical Profilometer, which provides a full 3D map image of the sample after scanning. This no-contact method splits a white light onto the sample and a reference mirror and uses the interference fringes resulting from the reflected beams to construct a map image. Figure 34 shows a diagram of an optical profilometer and Figure 35 features the Zygo ZeScope used in this research. The tool uses different interferometry modes depending on what type of sample is being scanned. The samples in this research are fairly smooth on the surface, so phase-shifting interferometry is used. In this mode, a piezoelectric transducer linearly moves the reference to cause a known phase shift, and the reflected beam intensity is converted to phase data and processed to remove variations [32].

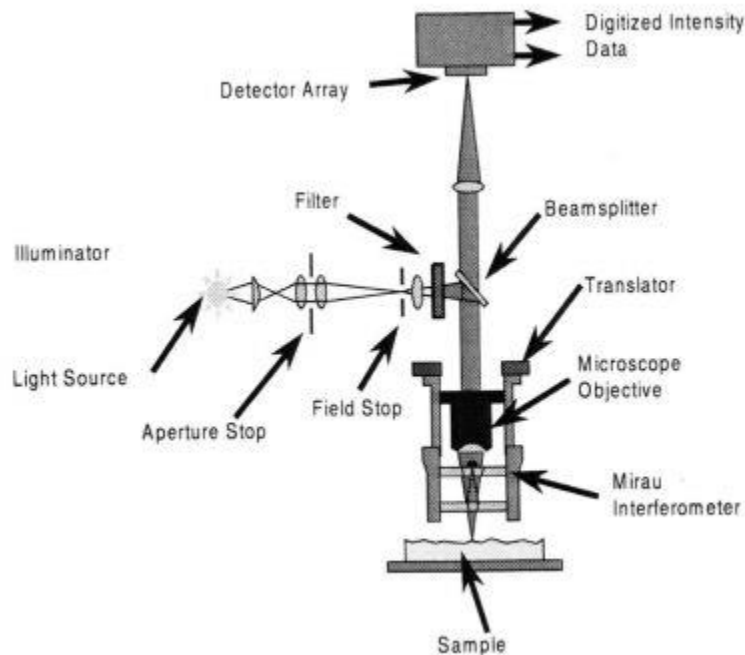


Figure 34: Diagram of optical profilometer components [32]

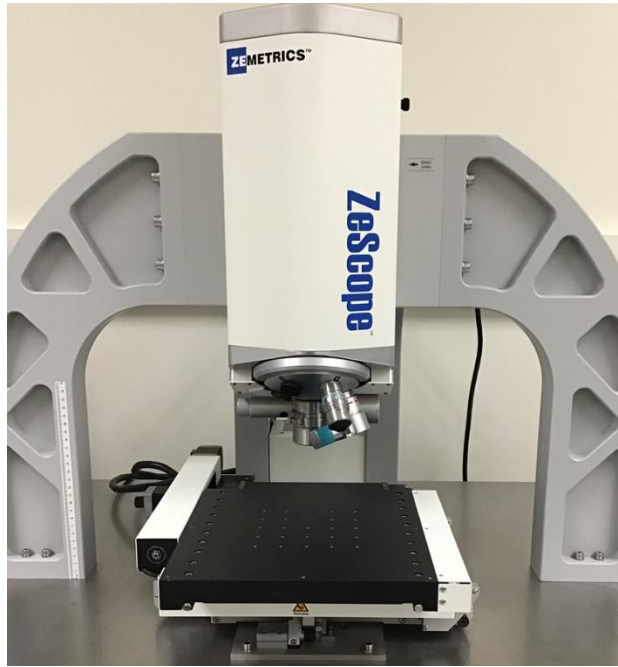


Figure 35: Zygo ZeScope optical profilometer system

3.3.4 Polarized Light Microscopy

Polarized light microscopy is a useful characterization technique to evaluate the anisotropic properties of the electrodeposit growth on the films. To accomplish this, a Mitutoyo FS110 microscope that is equipped with Mitutoyo polarizing units and an analyzer is used to view the samples. Figure 36 shows a diagram of a polarizing microscope, in which the light passes through a polarizer before passing through the sample, and the analyzer allows the user to adjust the contrast and brightness in order to best observe the sample features. Figure 37 is an image of the microscope used in this research.

Polarized Light Microscope Configuration

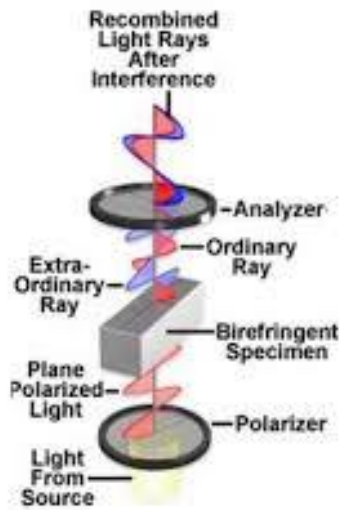


Figure 36: Diagram of light polarization in a polarizing microscope [32]

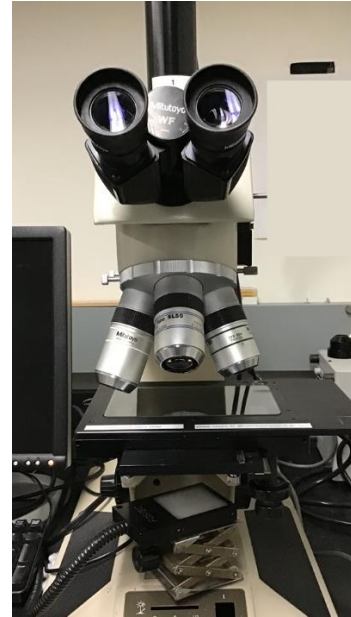


Figure 37: Mitutoyo FS110 microscope and polarizing system

This technique works by polarizing the light before it is incident on the sample such that the light experiences a phase change after passing through the sample, and the analyzer recombines the two phase components. This creates a view that clearly shows the constructive and destructive interference, or the topographic features of the sample [33]. Figure 38 shows how an electrodeposit growth feature looks both under a normal microscope and with a polarizing microscope.

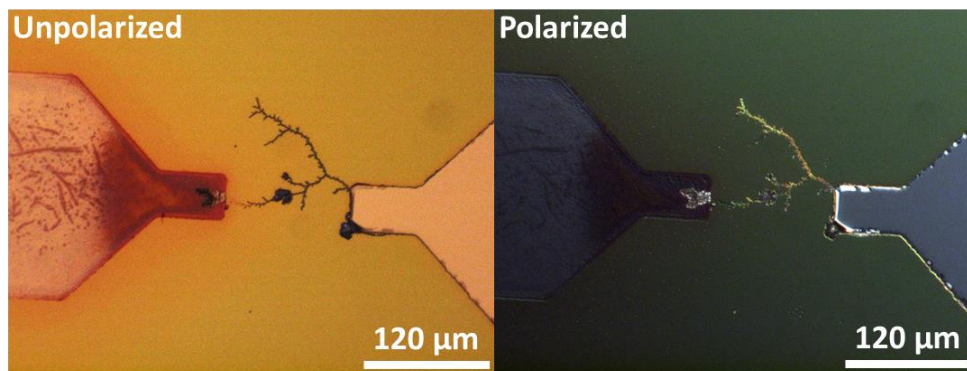


Figure 38: Electrodeposit growth on 60 nm $Ge_{30}Se_{70}$ + 10 nm Ag PMC device at 2 V and 95°C

CHAPTER 4

RESULTS AND DISCUSSION

4.1 Study of Electrodeposit Growth Rate

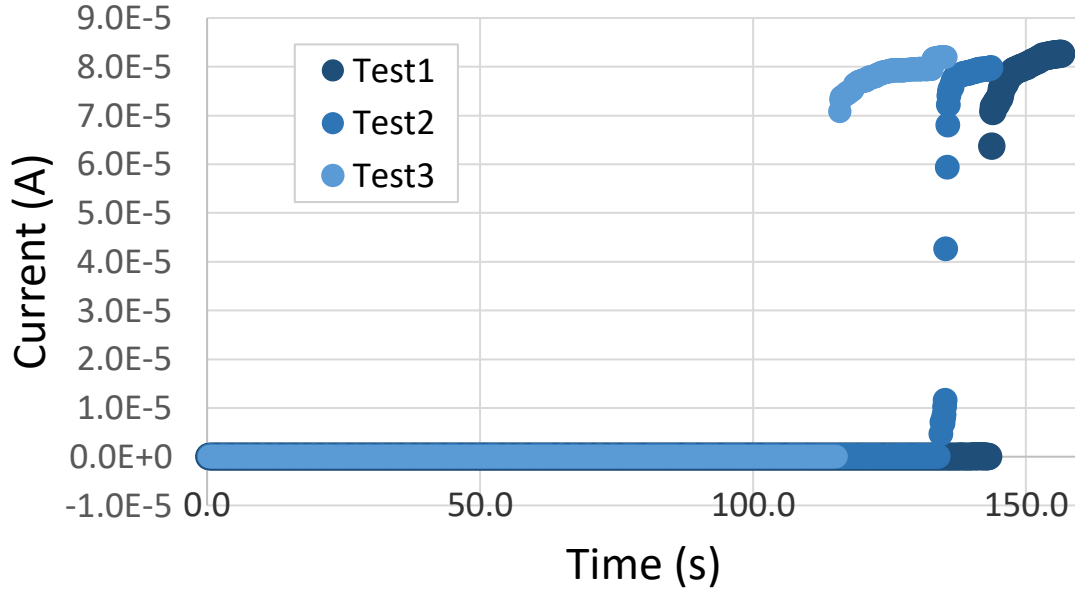
This study of the electrodeposit growth rate in lateral PMC devices considers several dependent variables, including electric field in the channel, electrolyte composition, and device temperature. Table 8 shows an outline of the tests performed in relation to composition, where three devices were tested in each category:

Table 8: Electrical characterization test categories for each PMC composition

Composition	Electrode Shape	Bias
<i>60nm Ge₃₀Se₇₀ + 10nm Ag</i>	Square	Constant 2V
		Constant 1V
	Sharp	Constant 2V
		Constant 1V
<i>60nm Ge₃₀Se₇₀ + 20nm Ag</i>	Square	Constant 2V
		Constant 1V
	Sharp	Constant 2V
		Constant 1V
<i>60nm Ge₃₀S₇₀ + 10nm Ag</i>	Square	Constant 2V
	Sharp	Constant 2V

The three devices in each test were usually within 10% of the average calculated time to short. Graph 1 shows the three 60nm Ge₃₀Se₇₀ + 10nm Ag devices with square electrodes tested at room temperature under 2V applied bias. The average time to short for this test was 131.45 seconds, and the maximum percentage a device strayed from this time is 10.21%. This trend holds true for most tests that yielded a connection between the

electrodes; as will be discussed, devices that could not form a connection exhibited less consistent growth and immeasurable “short times”.



Graph 1: Current-time plot of three 60nm Ge₃₀Se₇₀ + 10nm Ag lateral PMC devices at 20°C under 2V bias

4.1.1 Electrodeposit Growth Rate Results

Table 9 is a summary of the time it took for the electrodeposit to form a connection between the anode and the cathode, or the time to short, for each lateral PMC device category outlined above. The devices were tested at two temperatures ($T_1=20^\circ\text{C}$ and $T_6=95^\circ\text{C}$) and at two biases (2V and 1V), and the time to short is the average time from the three devices tested. A glossary of polarized and unpolarized micrographs for each device category can be found in Appendix A.

Table 9: Time to short summary for tested PMC devices at low and high temperature

<i>Lateral PMC Device</i>	<i>Time to Short (s)</i>	
	$T_1 = 20^\circ\text{C}$	$T_6 = 95^\circ\text{C}$
<i>60nm Ge₃₀Se₇₀ + 10nm Ag, 2V bias, square electrode</i>	131.45	39.58
<i>60nm Ge₃₀Se₇₀ + 10nm Ag, 2V bias, sharp electrode</i>	215.62	13.94
<i>60nm Ge₃₀Se₇₀ + 10nm Ag, 1V bias, square electrode</i>	∞	∞
<i>60nm Ge₃₀Se₇₀ + 10nm Ag, 1V bias, sharp electrode</i>	∞	∞
<i>60nm Ge₃₀Se₇₀ + 20nm Ag, 2V bias, square electrode</i>	78.93	11.98
<i>60nm Ge₃₀Se₇₀ + 20nm Ag, 2V bias, sharp electrode</i>	100.08	12.86
<i>60nm Ge₃₀Se₇₀ + 20nm Ag, 1V bias, square electrode</i>	∞	∞
<i>60nm Ge₃₀Se₇₀ + 20nm Ag, 1V bias, sharp electrode</i>	1161.00	208.00
<i>60nm Ge₃₀S₇₀ + 10nm Ag, 2V bias, square electrode</i>	969.87	308.56
<i>60nm Ge₃₀S₇₀ + 10nm Ag, 2V bias, sharp electrode</i>	881.87	1272.6

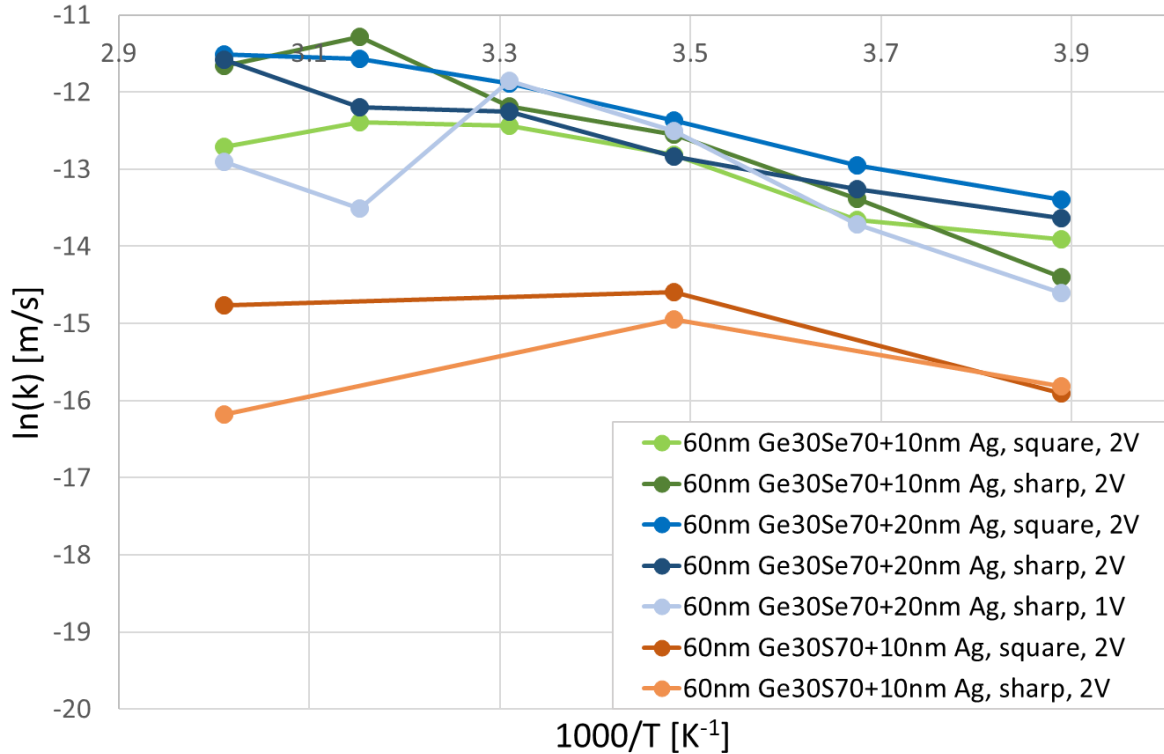
The devices with an infinite time to short never made a full connection between the electrodes. The experiments were run until the silver was completely depleted from the active silver anode, such that the current dropped to zero when the silver ions were no longer present. Thus, the time to short in these cases is best described as infinite. These

devices were also incapable of producing an activation energy value, as the “event” described in the Arrhenius equation was never completed. Table 10 shows a summary of the extracted activation energies from these lateral PMC devices based on the electrodeposit time to short:

Table 10: Summary of activation energies from tested PMC devices

Device	E_a (eV)
<i>60nm Ge₃₀Se₇₀ + 10nm Ag, square, 2V</i>	0.148
<i>60nm Ge₃₀Se₇₀ + 10nm Ag, sharp, 2V</i>	0.291
<i>60nm Ge₃₀Se₇₀ + 20nm Ag, square, 2V</i>	0.199
<i>60nm Ge₃₀Se₇₀ + 20nm Ag, sharp, 2V</i>	0.196
<i>60nm Ge₃₀Se₇₀ + 20nm Ag, sharp, 1V</i>	0.149
<i>60nm Ge₃₀S₇₀ + 10nm Ag, square, 2V</i>	0.148
<i>60nm Ge₃₀S₇₀ + 10nm Ag, sharp, 2V</i>	0.291

Graph 2 is a summary of the Arrhenius plots from which the activation energy values were found for the tested lateral PMC devices:



Graph 2: Arrhenius plot of the tested lateral PMC devices

4.1.2 Electrode posit Growth Rate Discussion

4.1.2.1 Channel Electric Field Effects

The electric field present in the device channel is affected by the electrode shape and the applied bias. The sharp electrodes nearly always have a longer time to short than the square electrodes, and this trend is further supported by smaller activation energies for square electrodes (except for the more highly-doped selenide-based device, whose activation energies are comparable for both electrode shapes).

The growth rate is expected to be faster between the square electrodes due to the smaller effective channel width; in recalling Equation 3, the electric field is inversely dependent on the channel width, such that decreasing the width increases the effective electric field in the channel. Because the sharp electrodes' channel width extends along the sides of the triangular tips, the electric field weakens when not directly between the two electrode tips. Figures Figure 39 and Figure 40 are good examples of how the electric field strength influences growth in the channel:

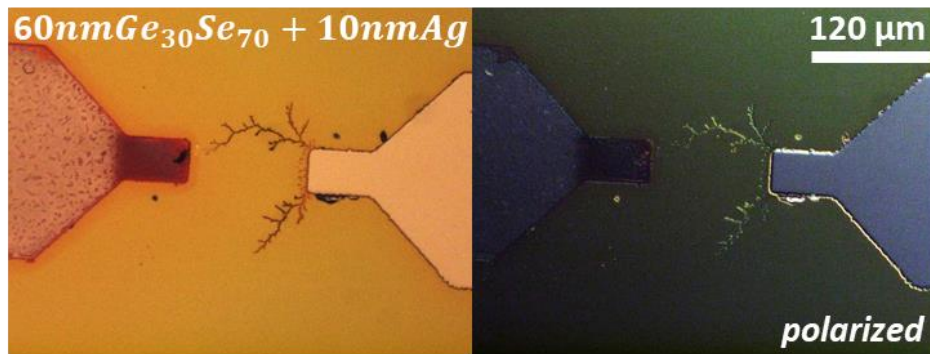


Figure 39: 60nm Ge₃₀Se₇₀ + 10nm Ag lateral PMC device at 20°C under 2V bias, square electrode

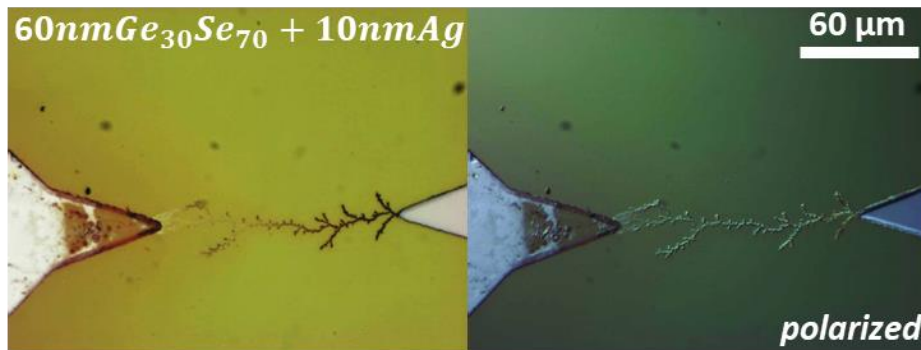
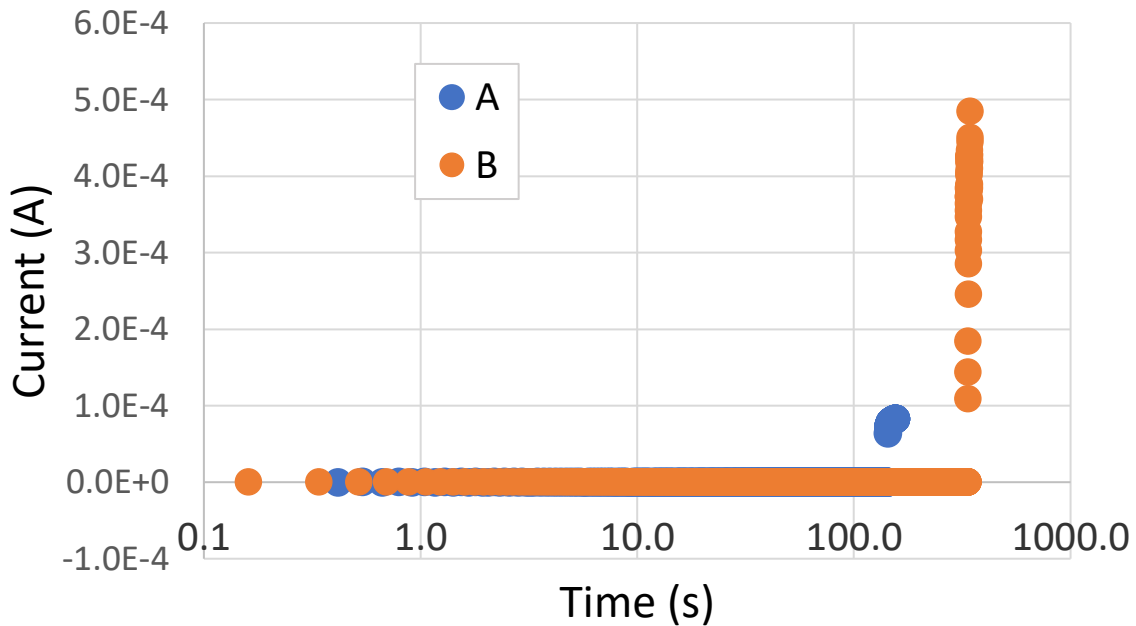


Figure 40: 60nm Ge₃₀Se₇₀ + 10nm Ag lateral PMC device at 20°C under 2V bias, sharp electrode

In Figure 39, the electrodeposit is not as confined to the channel between the electrodes as the electrodeposit in Figure 40 is. Because the free silver cations are under the influence of a stronger electric field in the square electrodes, they grow toward the

anode more quickly. For the most part, this trend holds true at higher temperatures as well. The electrodeposit growth mode is not affected by the electrode shape, and these devices exhibit mode 4 growth, with high mobility and low redox rates.

An interesting result is that although the sharp electrodes take longer to short, they tend to yield higher currents after shorting. Graph 3 of a 60nm Ge₃₀Se₇₀ + 10nm Ag, 2V, 20°C device shows the difference in magnitude of the shorted current, where the sharp electrode current is roughly five times greater. The plot shows the current in amps and the time in seconds on a log-scale. This can also be seen in Figure 40, where the polarized image highlights how the electrodeposit is denser than the electrodeposit in Figure 39, suggesting a lower overall resistance for electron flow.



Graph 3: Current-time plot of 60nm Ge₃₀Se₇₀ + 10nm Ag lateral PMC devices at 20°C under 2V bias

The applied bias also affects the electric field; referring to Equation 3 again, the electric field is directly dependent on the voltage. Thus, the results are consistent with the

expectation that the 2V bias yields faster times to short than the 1V bias in all cases. In fact, most devices are noted as having an “infinite” time to short because an electrodeposit connection between electrodes never occurred, even at high temperatures—this indicates that ion availability is the limiting factor.

Figure 41 shows a 60nm Ge₃₀Se₇₀ + 10nm Ag device grown until total silver depletion at 20°C under the 1V bias:

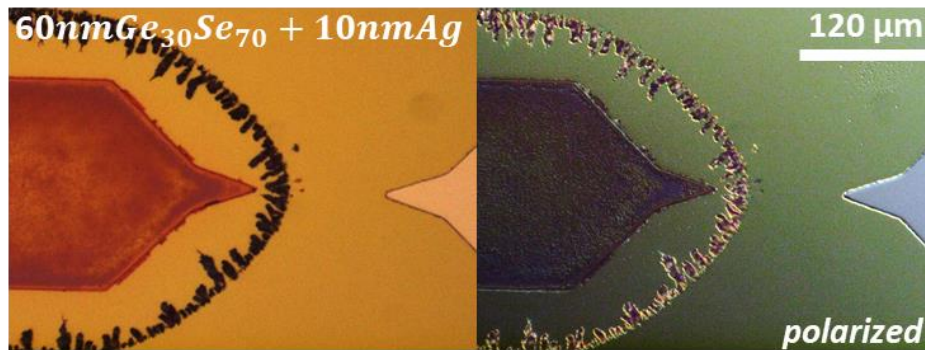


Figure 41: 60nm Ge₃₀Se₇₀ + 10nm Ag lateral PMC device at 20°C under 1V bias

In this device, a halo-growth effect occurs around the anode, where the electrodeposit grows toward the outside of the entire anode rather than strictly along the channel. This could be due to the low electric field causing ions to nucleate early within the channel, as the low field does not allow the ions to grow toward the anode quickly enough as the silver ions build up at the reduced cathode. This corresponds to growth mode 2, in which there is low mobility and a low redox rate. The discrete nanoclusters and cone shape around the anode indicative of this growth type are clearly visible in Figure 41, and this growth mode is present in the square electrode of this composition as well.

In the 60nm $\text{Ge}_{30}\text{Se}_{70}$ + 20nm Ag devices, the square electrode was not able to make a connection either, but the growth mode is less clear in this case. Figure 42 shows this device at 20°C under the 1V bias, where the electrodeposit is very diffuse within the electrolyte.

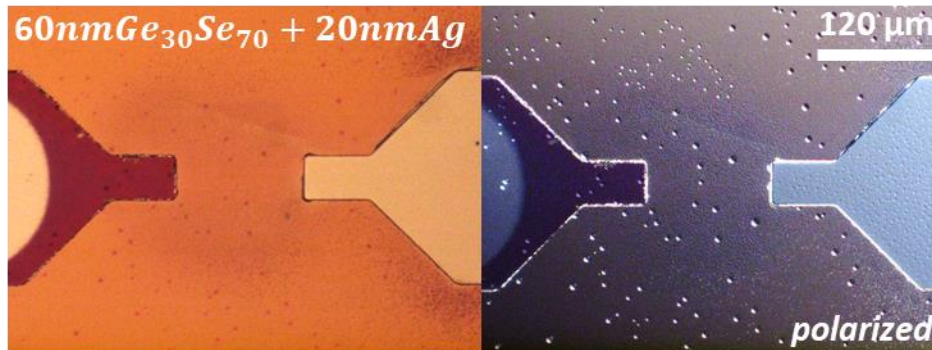
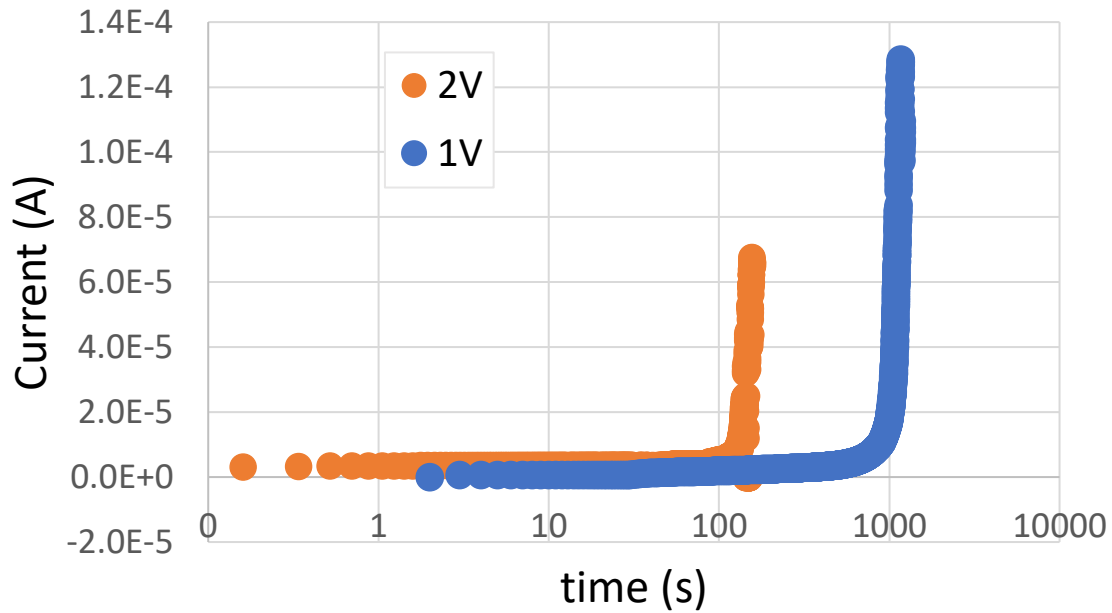


Figure 42: 60nm $\text{Ge}_{30}\text{Se}_{70}$ + 20nm Ag lateral PMC device at 20°C under 1V bias

The only device that could form a connection between the electrodes at 1V was the 60nm $\text{Ge}_{30}\text{Se}_{70}$ + 20nm Ag device with sharp electrodes. While the electrodeposit looks nearly identical to Figure 42 with the silver diffused in the electrolyte, the current-time results show the presence of a complete connection between electrodes:



Graph 4: Current-time plot of 60nm Ge₃₀Se₇₀ + 20nm Ag lateral PMC devices at 20°C

Interestingly, Graph 4 is reminiscent of Graph 3, where the device grown under lower electric field, while slower, yields a higher current after shorting.

4.1.2.2 Electrolyte Composition Effects

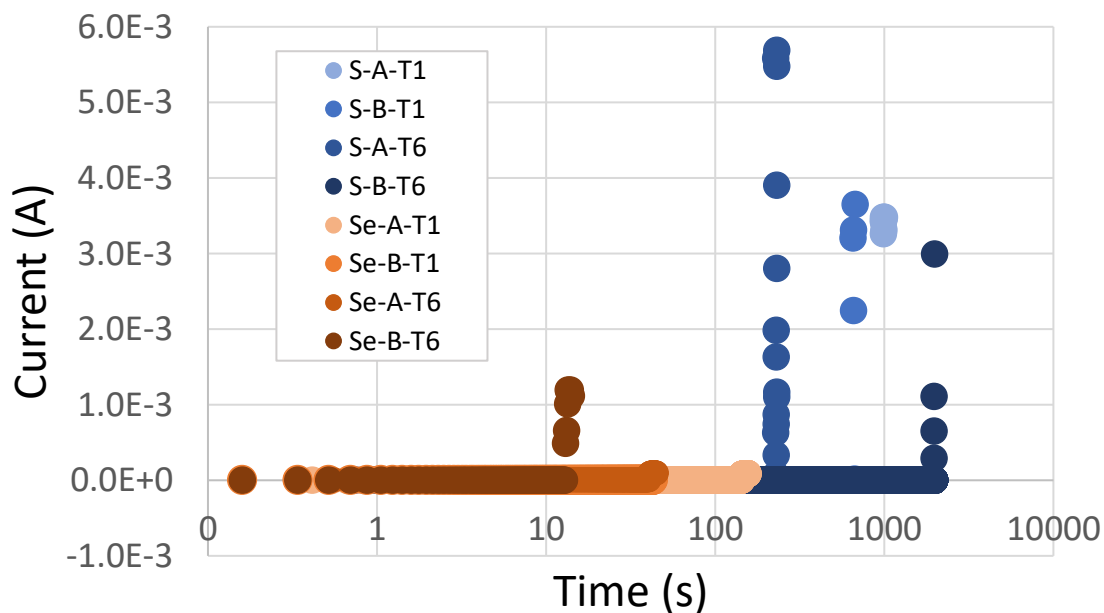
The compositions of the lateral PMC electrolytes were both varied in chalcogenide and in amount of silver doping. The two chalcogenides evaluated are selenide and sulfide-based, or 60nm Ge₃₀Se₇₀ + 10nm Ag and 60nm Ge₃₀S₇₀ + 10nm Ag. Because these device compositions are doped with the same amount of silver, it is reasonable to assign electrodeposit growth variance on the different chalcogen element.

Overall, both compositions exhibit similar growth modes in this comparison; the square electrodes cause the Y-shaped electrodeposit and both devices yield a dendritic-like form. The polarized images also suggest both devices had growth that exists on top

of the electrolyte. Thus, both devices exhibit mode 4 growth, with high cation mobility and low redox rates.

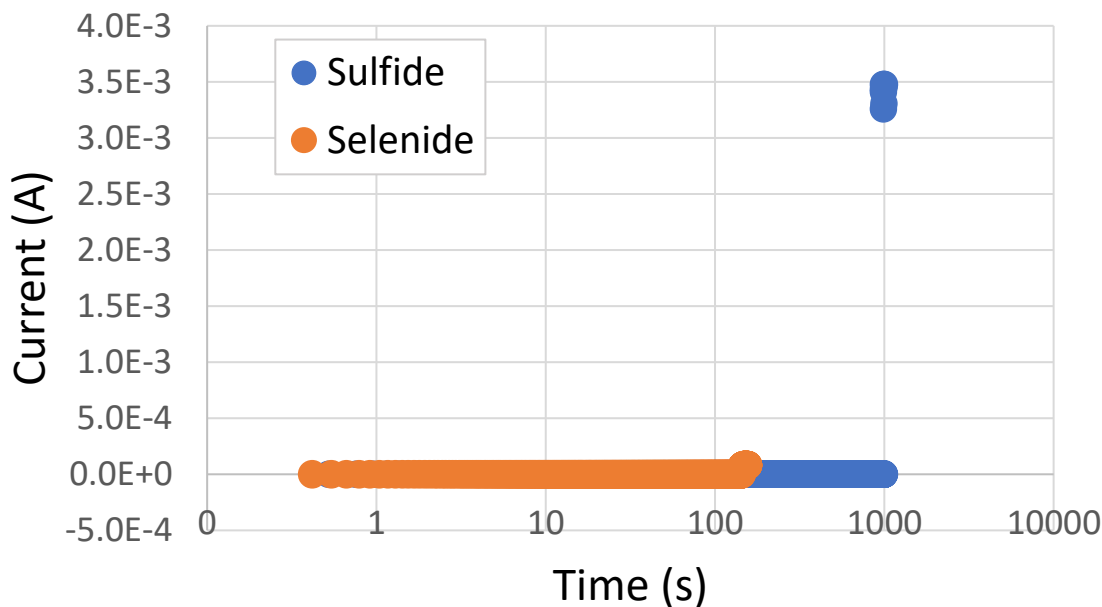
The sulfide-based composition's time to short is nearly an order of magnitude larger than the selenide-based composition for both electrode shapes and at both room and high temperature. This confirms that sulfide-based germanium chalcogenides are more relaxed in structure than selenide-based germanium chalcogenides and that germanium-sulfide chalcogenides have an ion mobility nearly an order of magnitude lower than the germanium-selenide counterparts [13], [14].

The Arrhenius plot in Graph 2 also shows the stark difference between sulfide-based and selenide-based chalcogenides. The sulfide-based plot, while similar in shape to the selenide-based plots, exists 2-4 m/s below the selenide-based plots. Graph 5 shows the difference in current-time behavior for these two compositions for devices grown under 2V applied bias, where the sulfide-based devices are shown in blue and selenide-based devices are in orange; both square (A) and sharp (B) electrodes are shown at 20°C (T1) and 95°C (T6):



Graph 5: Current-time plot of 60nm Ge₃₀Se₇₀ + 10nm Ag and 60nm Ge₃₀S₇₀ + 10nm Ag lateral PMC devices at 20°C and 95°C under 2V bias for both electrode shapes

It is clear here that the sulfide-based devices are consistently slower than the selenide-based devices, and that the current upon forming a connection is higher in the sulfide-based devices. Graph 6 exemplifies this difference in the two compositions at room temperature: the sulfide-based device is 7.4 times slower than the selenide-based devices, but the current after shorting is over 42 times higher in the sulfide-based device. Once again, this continues the trend that the electrodeposits grown more slowly yield a larger current upon connection.



Graph 6: Current-time plot of 60nm Ge₃₀Se₇₀ + 10nm Ag and 60nm Ge₃₀S₇₀ + 10nm Ag lateral PMC devices at 20°C under 2V bias

The composition was also varied by increasing the amount of silver doping, specifically in the selenide-based chalcogenides, where 60nm Ge₃₀Se₇₀ + 10nm Ag and 60nm Ge₃₀Se₇₀ + 20nm Ag devices were tested. From Table 9, it is clear than when the equivalent devices are compared, the compositions doped with 20nm Ag are always faster than the 10nm Ag counterparts. This is likely due to a higher presence in silver ions, and the existing silver nanoclusters can contribute to form conductive paths for even faster ion transport [9].

The 10nm Ag composition exhibits the mode 4 growth mode with high mobility, low redox rates, demonstrated in Figure 39. The 20nm Ag compositions did not grow strong, metallic electrodeposit growth, but a more subdued, diffused growth. Figure 43 gives insight into this phenomenon, where the dimples in the film might indicate an oxide layer or perhaps improper diffusion of silver. Some research shows that nanoclusters can migrate during the electrochemical reaction process and form a “void” around the

cathode [16]. This makes sense, as this device composition has a higher concentration of silver and it is possible that the silver was not fully diffused. It is possible that this growth mode can be described as mode 1, with both high mobility and high redox rates, due to the excess in silver cations, in combination with nanocluster migration modes.

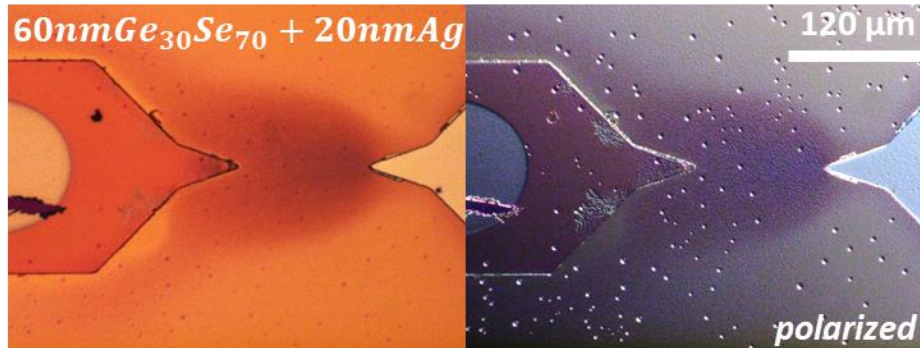


Figure 43: 60nm $\text{Ge}_{30}\text{Se}_{70}$ + 20nm Ag lateral PMC device at 20°C under 2V bias

4.1.2.3 Device Temperature Effects

These devices were tested at room temperature and up to 95°C to evaluate the effects of high temperature on the electrodeposit growth. Time to short decreases by nearly an order of magnitude at 95°C for almost all devices tested. Figure 44 shows an example of high-temperature growth in selenide-based devices, where the electrodeposit yields thicker, more protrusive growth. This could be because the high temperature increases ion mobility and the redox reaction rate, allowing more ions to flow to the cathode and nucleate quickly. In the 60nm $\text{Ge}_{30}\text{Se}_{70}$ + 10nm Ag composition, the devices exhibit a combination of mode 1 and mode 4 growth, where both have high mobility, but mode 1 has high redox rates and mode 4 has low redox rates. The branch-like electrodeposit suggests the mode 4 growth, similar to the room temperature case, but the density of the electrodeposit suggests higher redox rates and mode 1-like growth.

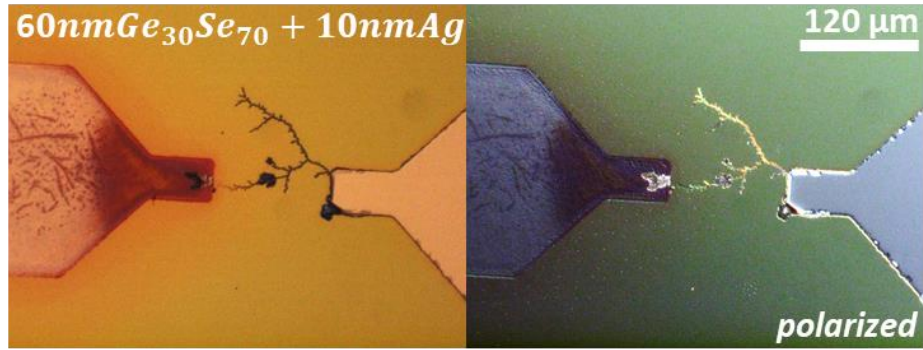


Figure 44: 60nm $\text{Ge}_{30}\text{Se}_{70}$ + 10nm Ag lateral PMC device at 95°C under 2V bias

Because selenide-based chalcogenides experience a phase change near this high temperature, it further supports the idea that the silver cation transport changes in the electrolyte. In particular, the 60nm $\text{Ge}_{30}\text{Se}_{70}$ + 20nm Ag composition, which at 20°C displayed mode 1 and nanocluster migration growth modes, undergoes a drastic change when heated to 95°C. In comparison to Figure 43, Figure 45 displays a much more mode 4-like electrodeposit. While there still seems to be silver diffusion within the electrolyte, hinting at the presence of the nanocluster migration growth mode, the effects from the high temperature on the material composition are clear. Graph 7 is further evidence of this composition change.

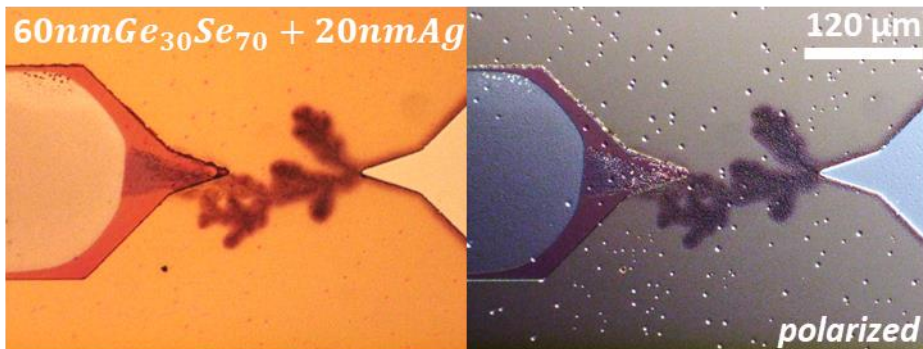
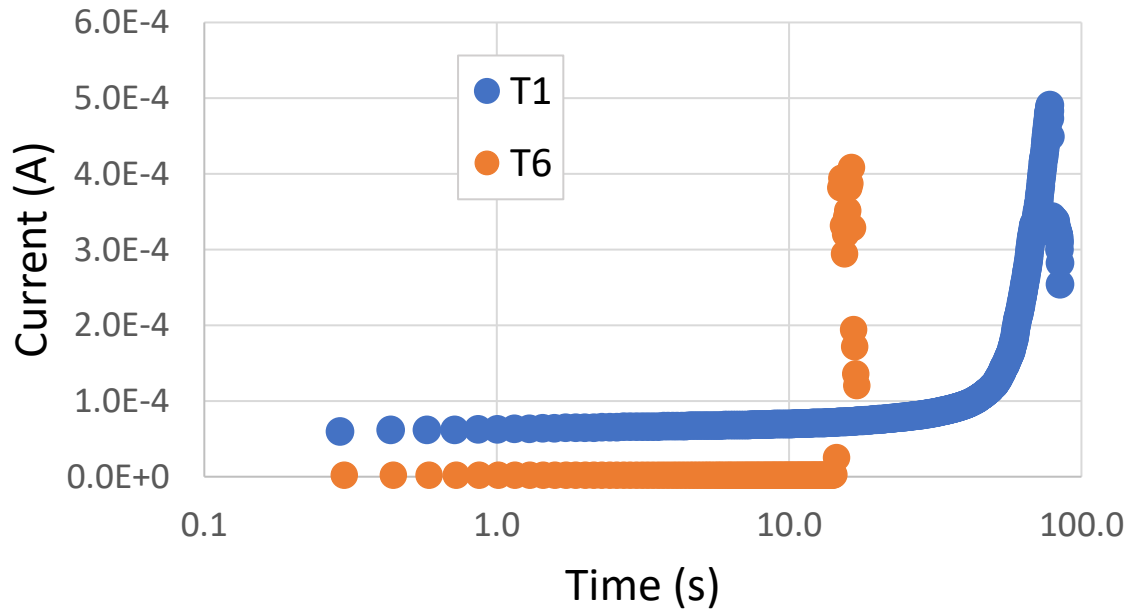


Figure 45: 60nm $\text{Ge}_{30}\text{Se}_{70}$ + 20nm Ag lateral PMC device at 95°C under 2V bias

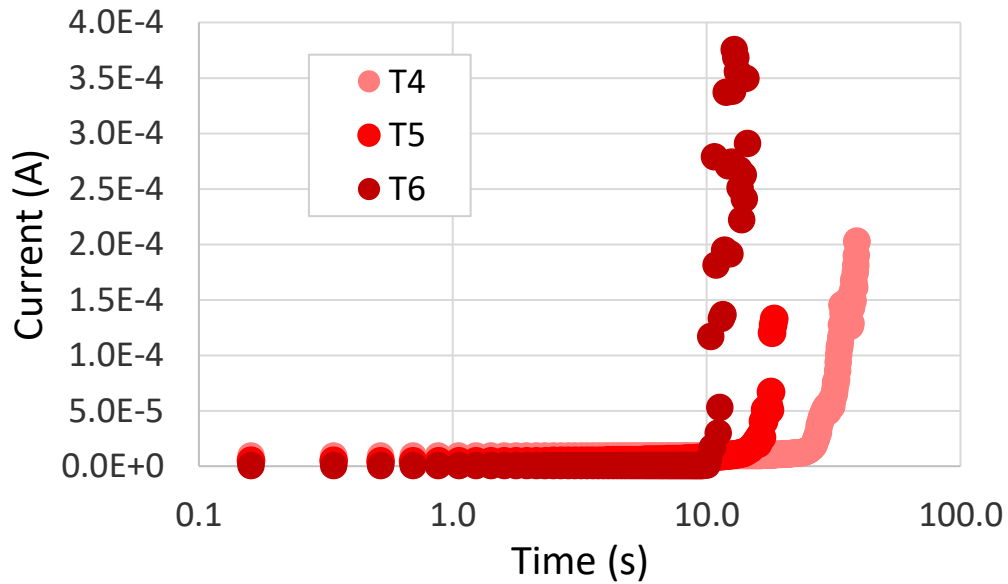


Graph 7: Current-time plot of 60nm Ge₃₀Se₇₀ + 20nm Ag lateral PMC devices at 20°C and 95°C under 2V

At room temperature, the growth is coupled with a higher starting current and a slow curve up to the current after a connection is made. After being heated to 95°C, the starting current is low, on the order of a nanoamp—a consistent value across other selenide-based devices—and exhibits the more expected delta-function jump when a connection is made. This change in current is evidence that the growth mode is less dominated by nanocluster migration, which can contribute to the higher starting current. This phenomenon occurred in this same device category at 1V bias as well.

In order to verify when this phase change occurs in these selenide-based devices, a comparison is made below at three high temperatures: 65°C, 80°C, and 95°C. From Graph 8, it is clear that the time to short decreases as the temperature increases, from roughly 40 seconds to 20 seconds to 12 seconds, respectively. However, only at 95°C does the current-time curve appear to exemplify the behavior of the delta-function jump

upon shorting. This is indicative of the phase change occurring at some temperature after 80°C, as this phase change does not seem to occur. Figure 46 further supports this, where at 65°C and 80°C, the diffuse silver nanocluster migration growth mode seems to dominate, and only at 95°C does the more mode 4-like growth occur.



Graph 8: Current-time plot of 60nm Ge₃₀Se₇₀ + 20nm Ag lateral PMC devices at 65°C (T4), 80°C (T5), and 95°C (T6) under 2V

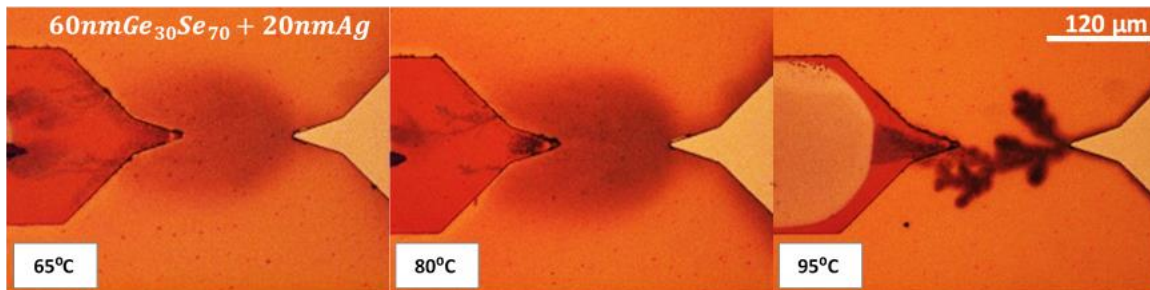


Figure 46: 60nm Ge₃₀Se₇₀ + 20nm Ag lateral PMC device at 65°C, 80°C, and 95°C under 2V bias

To further investigate the changes occurring in the 60nm Ge₃₀Se₇₀ + 20nm Ag composition, the devices were heated to 95°C for 30 minutes and subsequently cooled to 20°C; the devices exhibited different growth modes at room temperature after being heat-

treated. While Figure 43 shows the electrodeposit growth of this composition at room temperature and Figure 45 shows the device at 95°C, Figure 47 shows this device at room temperature after heat treatment:

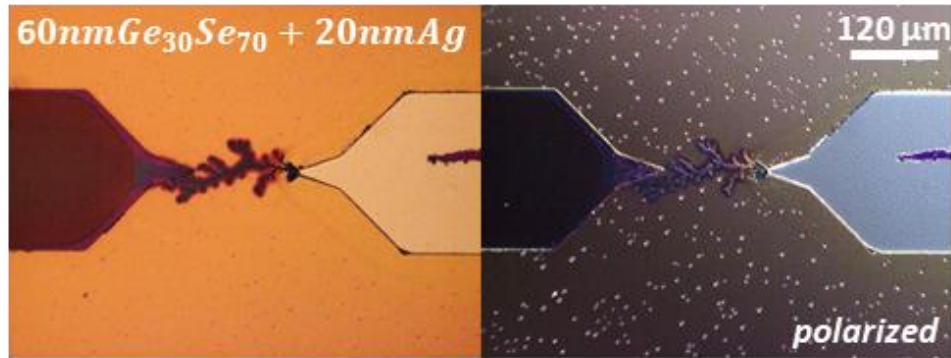
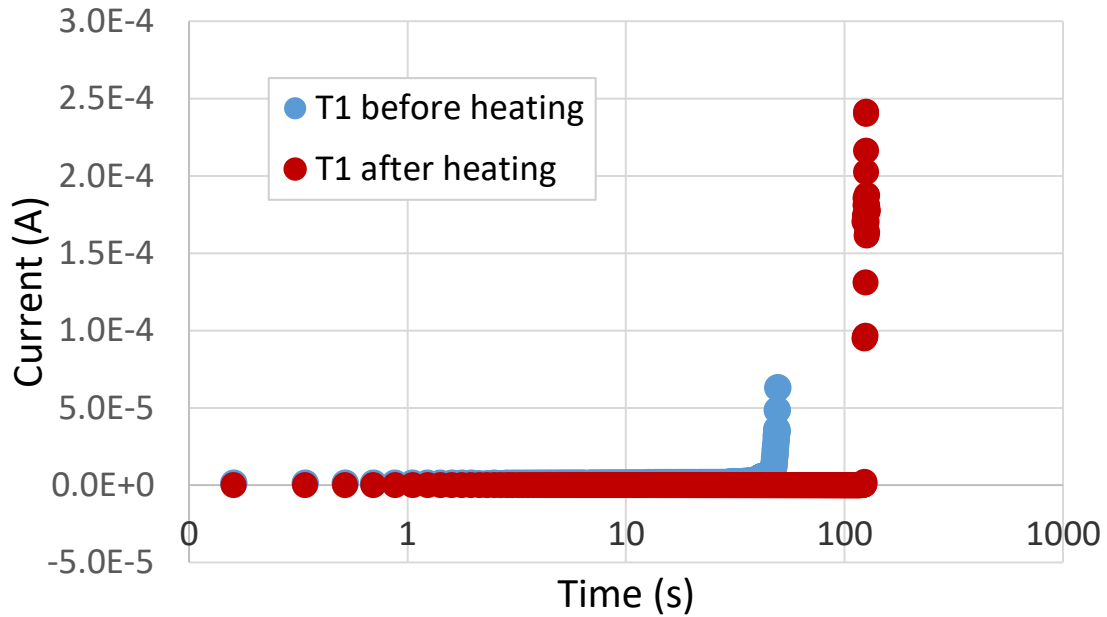


Figure 47: 60nm $\text{Ge}_{30}\text{Se}_{70}$ + 20nm Ag lateral PMC device at 20°C under 2V bias after heat-treatment

The electrodeposit looks remarkably similar to the growth from this device at high temperatures despite being grown at room temperature. While the pre-heat-treated device exhibits mode 1 and nanocluster migration growth behaviors, both the high temperature and heat-treated devices exhibit mode 4 and nanocluster migration growth. This supports the idea that a compositional phase change occurred in this chalcogenide in such a way that the ion transport at room temperature resembles the transport at high temperature. In addition, the heat-treated devices took longer to form a connection between electrodes at room temperature than pre-heat treatment, as well as yielded a larger current after connection, which is demonstrated in Graph 9:



Graph 9: Current-time plot of 60nm Ge₃₀Se₇₀ + 20nm Ag lateral PMC device at 20°C under 2V bias after heat treatment

The sulfide-based device with square electrodes also experienced a decrease in time to short when grown at higher temperatures, but there is no change in growth mode. This makes sense, because while the increased temperature can contribute to increasing the redox rate to speed up the electrodeposit growth, the sulfide-based chalcogenides do not experience a phase change at 95°C.

However, the sulfide-based devices with sharp electrodes are the only instance in which the time to short increased at the higher temperature state. The main explanation for this over 140% increase in time to short is that the higher temperature also increases oxidation within films, and this device may be particularly sensitive to that oxidation. It is known that oxidation will slow down the growth of these devices, and perhaps because the device was so slow to begin with, the oxidation took over at 95°C. Interestingly, this slow growth allowed the electrodeposit to branch in such a way that it nearly resembles

the halo-effect around the active anode, shown in Figure 41, which suggests the silver ions were nucleating early within the channel [16]. Thus, this growth might be a mix between mode 4 and mode 2 growth modes.

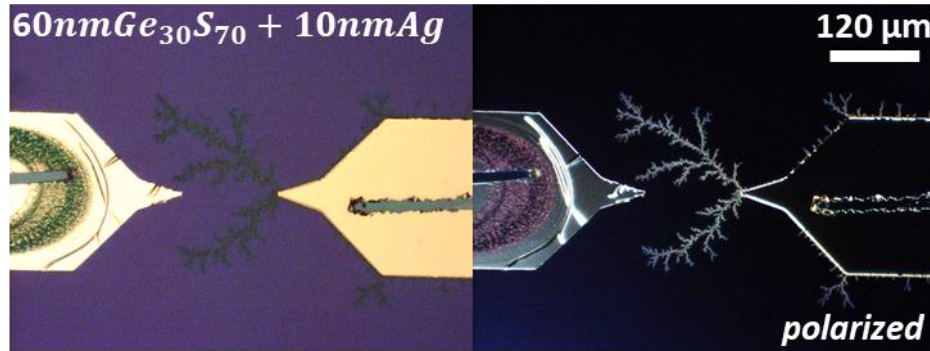


Figure 48: 60nm $\text{Ge}_{30}\text{S}_{70}$ + 20nm Ag lateral PMC device at 20°C under 2V bias after heat treatment

4.2 Optical Characterization

Optical characterizations were done to provide extra insight into the characteristics of the doped chalcogenides. Some extra characterizations were performed on thin film chalcogenides that underwent ionization radiation treatment, as the lateral PMC devices have applications that may expose the devices to excessive radiation.

4.2.1 Optical Characterization Results

Table 11 summarizes all of the extracted bandgap energy values for the tested compositions and compares them with accepted values in literature:

Table 11: Summary and comparison of bandgap values from tested compositions

Composition	Treatment	Extracted Bandgap (eV)	Literature Bandgap* (eV)
60nm Ge₃₀Se₇₀		2.873	2.06 [12]
60nm Ge₃₀Se₇₀ + 10nm Ag		1.715	1.88 [12]
60nm Ge₃₀Se₇₀ + 20nm Ag		0.441	1.64 [12]
60nm Ge₃₀Se₇₀ + 30nm Ag	<i>Photodoping</i>	0.919	1.55 [12]
60nm Ge₃₀Se₇₀ + 30nm Ag	<i>Photodoping + 1 Mrad</i>	0.771	
60nm Ge₃₀Se₇₀ + 30nm Ag	<i>Photodoping + 85°C</i>	0.406	
200nm Ge₃₀Se₇₀		1.319	2.21 [34]
200nm Ge₃₀Se₇₀ + 20nm Ag		1.080	
60nm Ge₃₀S₇₀		1.726	1.18 [14]
60nm Ge₃₀S₇₀ + 10nm Ag		1.167	
60nm Ge₃₀S₇₀ + 20nm Ag		1.174	
60nm Ge₃₀S₇₀ + 30nm Ag		0.658	
60nm Ge₄₀S₆₀		2.182	
60nm Ge₄₀S₆₀ + 30nm Ag		1.108	
60nm Ge₄₀S₆₀ + 30nm Ag	<i>Photodoping</i>	1.044	
60nm Ge₄₀S₆₀ + 30nm Ag	<i>Photodoping + 100 krad</i>	1.097	
60nm Ge₄₀S₆₀ + 30nm Ag	<i>Photodoping + 300 krad</i>	1.184	
60nm Ge₄₀S₆₀ + 30nm Ag	<i>Photodoping + 600 krad</i>	1.262	
60nm Ge₄₀S₆₀ + 30nm Ag	<i>Photodoping + 1 Mrad</i>	0.480	
60nm Ge₄₀S₆₀ + 30nm Ag	<i>Photodoping + 450°C</i>	-	

*Compositions are approximated based on estimated amount of silver deposited

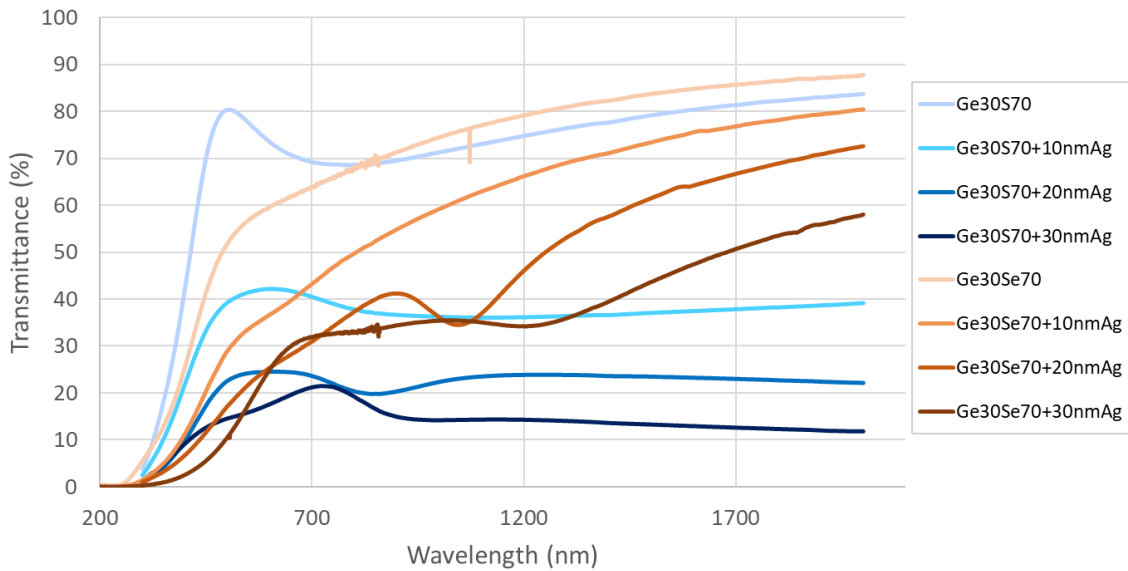
The thickness values used to calculate the bandgap energies can be found in Appendix B.

4.2.2 Optical Characterization Discussion

Overall, the bandgap energy value decreases as silver doping content increases in the thin films, for both selenide-based and sulfide-based chalcogenides, which is consistent with literature [11], [12]. Due to the increase in density of silver nano-clusters

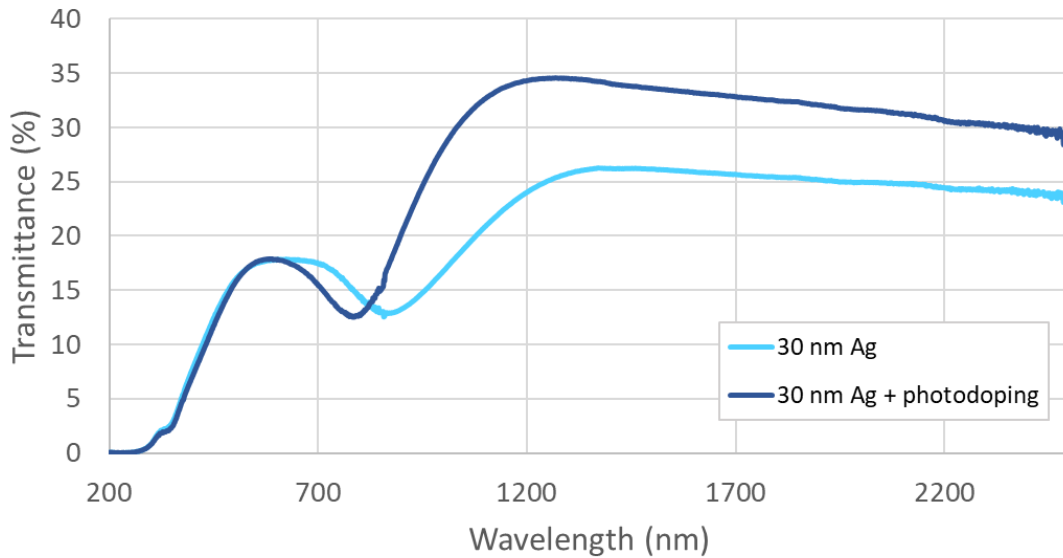
that occur in silver-doped chalcogenide films, the probability of exciting an electron to the conduction band increases because silver is a good supplier of electrons [9].

The extracted bandgap values for undoped chalcogenide layers tend to be higher than those values found in literature, while the silver-doped bandgap values tend to align more closely with values found in literature. The values cited are also extracted from much thicker films (on the order of 700 nm) or bulk materials, which may contribute to a difference in bandgap value. While a wide range of samples were examined in this UV-Vis spectrophotometry study, the most pertinent to the devices in this research are the silver-doped 60nm $\text{Ge}_{30}\text{Se}_{70}$ and 60nm $\text{Ge}_{30}\text{S}_{70}$ films. A more comprehensive investigation of this topic can be found in the undergraduate thesis “Optical Characterization of Silver-Doped Germanium-Chalcogenide Thin Films” [10]. The transmittance spectra from relevant compositions are shown in Graph 10:



Graph 10: Transmittance spectra of 60nm $\text{Ge}_{30}\text{Se}_{70}$ and 60nm $\text{Ge}_{30}\text{S}_{70}$ lateral PMC devices doped with silver

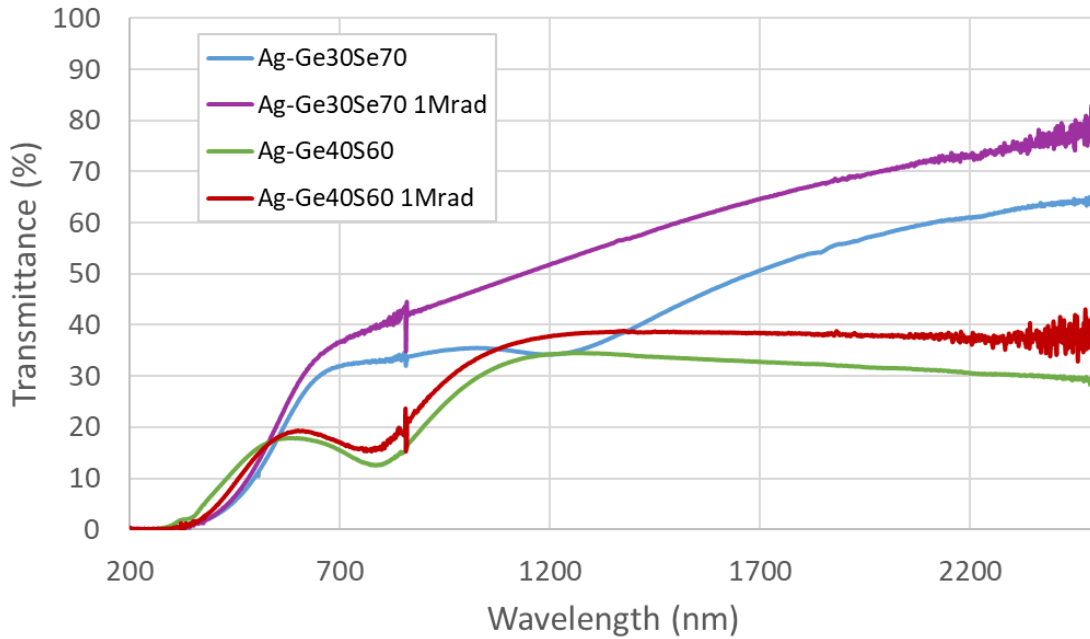
The effects of photodoping were also investigated using UV-Vis spectrophotometry, where one 60nm Ge₄₀S₆₀ + 30nm Ag thin film was exposed to UV light for 30 minutes after chalcogenide and silver deposition, and one 60nm Ge₄₀S₆₀ + 30nm Ag thin film was not exposed to UV light at all. Graph 11 shows the difference in transmittance spectra between the two samples:



Graph 11: Transmittance spectra of 60nm Ge₄₀S₆₀ + 30nm Ag lateral PMC devices

From Table 11, the photodoped film has a bandgap value of 1.044 eV and the un-photodoped film has a bandgap value of 1.108 eV. Interestingly, the photodoped composition actually has a slightly higher transmittance percentage than the un-photodoped composition in the low-energy region. This is likely due to the fact that photodiffusion causes the silver atoms to form tertiary compounds with the germanium and sulfur atoms, leading to different optical properties than metallic silver.

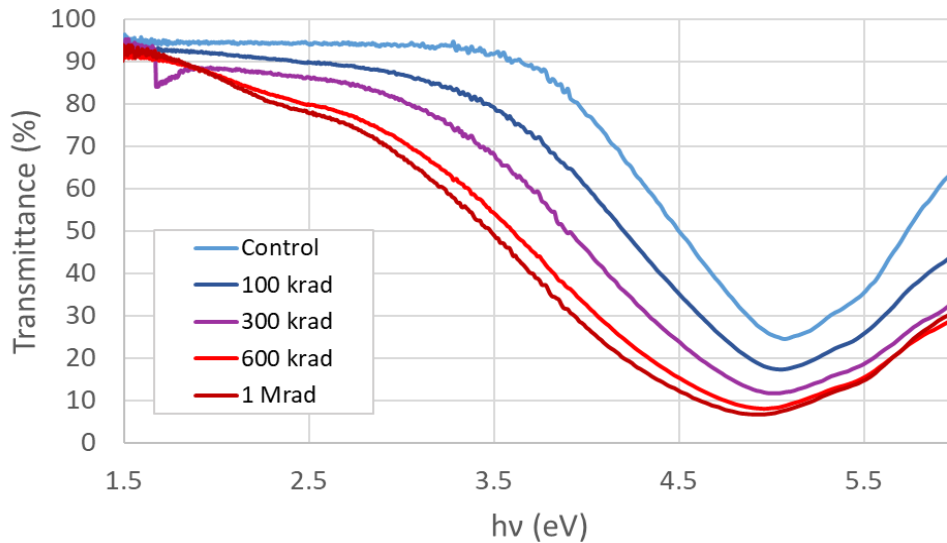
To investigate the effects of radiation on the compositions, a 60nm $\text{Ge}_{30}\text{Se}_{70}$ + 30nm Ag and a 60nm $\text{Ge}_{40}\text{S}_{60}$ + 30nm Ag (both photodoped) were exposed to 1 Mrad radiation treatment. The transmittance spectra are shown in Graph 12:



Graph 12: Transmittance spectra versus wavelength for 60nm $\text{Ge}_{30}\text{Se}_{70}$ and $\text{Ge}_{40}\text{S}_{60}$ Ag-doped films under radiation

The transmittance plots show that the radiation-treated films exhibit slightly higher transmittance properties as well as excess noise in the high energy region. It is interesting to note that the sulfide-based films display a similar transmittance curve after radiation exposure, if only slightly higher transmittance. The selenide-based films actually display a change in the transmittance curve, especially in the low-energy region. The extracted bandgap values show that both compositions experience a decrease in bandgap value after undergoing radiation treatment.

The final comparison simply evaluates the effects of radiation on the glass slides used in this research. Because the slides are meant to be nearly 100% transparent in the UV-Vis range such that they do not affect the spectrophotometry results, it is important to understand how the slides may be compromised due to these treatments.



Graph 13: Transmittance versus energy spectra of glass slides under degrees of radiation exposure

Graph 13 clearly shows that transmittance in the glass slide decreases as it is exposed to more radiation. In fact, Figure 49 shows the yellowing effect radiation has on the glass slides, an indication of them becoming less transparent.

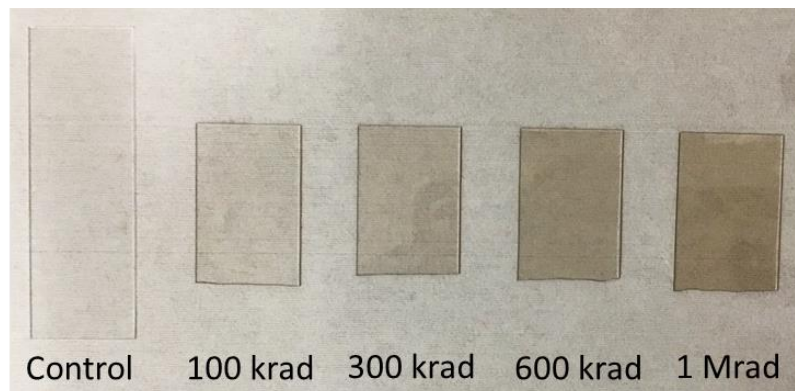


Figure 49: Yellowing effects of radiation on glass slides

4.3 Discussion

Coupling the electrical and optical characterization results is useful to have a well-rounded understanding of the devices and their materials. This research found that germanium-selenide chalcogenides yield faster electrodeposit growth than germanium-sulfide chalcogenides under the same conditions, even though they both exhibit mode 4 growth with high cation mobility and low redox rates. Additionally, the germanium-sulfide chalcogenides tend to have lower bandgap values than the germanium-selenide chalcogenides, which may suggest that cation transport is the main limiting factor in these materials.

Devices higher in silver content yielded faster electrodeposit growth and more varied growth modes; this presents a tradeoff in which the faster devices exhibited mode 1 and nanocluster migration growth mechanisms, which lead to very diffuse electrodeposits within the electrolyte. Further, the bandgap values of the chalcogenides consistently decrease as they are doped with more silver, for both germanium-selenide and germanium-sulfide compositions.

While the germanium-sulfide devices remained stable in the range of temperatures tested, the germanium-selenide devices experienced phase changes at 95°C that persist even after the material is cooled back to room temperature. While the change yielded faster growth at high temperature, the growth modes tended to be more mode-1 like, with higher redox rates creating denser electrodeposit growth. In fact, the more highly silver-doped germanium-selenide devices exhibited strong nanocluster migration growth mechanisms and lead to depletion regions to form around the active anode, which is more mode-2 like.

CHAPTER 5

CONCLUSIONS

To summarize, the purpose of this research was to investigate the electrical and optical properties of the materials that novel PMC devices are based on. In particular, the lateral PMC devices are constructed in such a way that the electrically-controlled electrodeposition growth has a measurable time-dependency such that the device can serve as an integrable timer for security and anticounterfeiting purposes.

The timing devices are dictated by solid-state electrochemical reactions which rely on a carefully-selected electrolytic layer. From this research, it appears the 60nm $\text{Ge}_{30}\text{S}_{70}$ + 10nm Ag composition best functions as the electrolyte for the timers; this composition, although slow, yielded the most consistent growth, remaining in growth mode 4 regardless of electrode shape or temperature effects. The stability of this material would serve as a reliable and predictable electrolyte for timers, and the speed of growth can be easily increased by amplifying the electric field, whether by decreasing electrode spacing or increasing applied bias.

It is important to consider different operating temperatures in different applications, however. For example, commercial electronics applications cover a range from 0-70°C and industrial applications from -40-85°C [35]. Thus, the selenide-based devices might serve well in metering for commercial and industrial applications, as long as the silver nanocluster migration growth mode is not dominating. In military and aerospace electronics applications, the accepted operating temperature range is from -55-125°C, in which case the sulfide-based devices would be required due to their thermal stability over 95°C [36]. Finally, in low earth orbit space applications, the temperature

range is from -170-120°C, which would again call for the sulfide-based devices [37]; however, the electronics in space applications are exposed to radiation, which have a clear effect on these materials' bandgap and other optical properties.

CHAPTER 6

FUTURE WORK

Future work would include using a scanning electron microscope (SEM) to perform a compositional analysis on these materials to find the exact atomic percentage of silver. Specifically, it would be useful to discover the exact atomic percentages of silver doping amount in the blanket chalcogenide film and in the channel of the devices after growth. This would be especially interesting for the 60nm Ge₃₀Se₇₀ + 20nm Ag devices that exhibit the nanocluster migration growth modes. This compositional analysis could also unveil interesting information about the phase changes that occur in the selenide-based devices after being heated to 95°C.

Other work that can be done is testing the sulfide-based devices at higher electric field, whether by testing the devices at smaller electrode spacing or at higher applied biases. This would be important to test the limits of the growth mode stability in these devices. To that end, testing the sulfide-based devices at even higher temperatures would be helpful—some limitations due to available high-temperature probestations may arise for these tests.

REFERENCES

- [1] Valov, R. Waser, J. R. Jameson, and M. N. Kozicki, “Electrochemical metallization memories—fundamentals, applications, prospects,” *Nanotechnology*, vol. 22, no. 28, p. 289502, Jul. 2011, doi: 10.1088/0957-4484/22/28/289502.
- [2] F. Pan, S. Gao, C. Chen, C. Song, and F. Zeng, “Recent progress in resistive random access memories: Materials, switching mechanisms, and performance,” *Materials Science and Engineering: R: Reports*, vol. 83, pp. 1–59, Sep. 2014, doi: 10.1016/j.mser.2014.06.002.
- [3] M. N. Kozicki and H. J. Barnaby, “Conductive bridging random access memory—materials, devices and applications,” *Semiconductor Science and Technology*, vol. 31, no. 11, p. 113001, Nov. 2016, doi: 10.1088/0268-1242/31/11/113001.
- [4] M. N. Kozicki, “Timing Device Using Electrodeposit Growth,” United States Patent 20180259911, Oct. 5, 2016.
- [5] Y. Gonzalez Velo, M. N. Kozicki, D. Chang, A. Odishvili, and E. Mikkola, “Timing Devices Based on the Growth of Metal Electrodeposit,” GOMAC Tech proceedings, 2017.
- [6] Y. Gonzalez Velo, “Integrated Circuit Authentication and Reliability Tool and Techniques,” DOD Phase 1 and Phase 2 Proposals #AF topic 16.1-141.
- [7] “Chalcogens and Chalcogenides,” *Chemistry LibreTexts*, 14-Aug-2020. [Online]. Available: [https://chem.libretexts.org/Bookshelves/Inorganic_Chemistry/Book%3A_Inorganic_Chemistry_\(Saito\)/04%3A_Chemistry_of_Nonmetallic_Elements/4.05%3A_Chalcogens_and_Chalcogenides](https://chem.libretexts.org/Bookshelves/Inorganic_Chemistry/Book%3A_Inorganic_Chemistry_(Saito)/04%3A_Chemistry_of_Nonmetallic_Elements/4.05%3A_Chalcogens_and_Chalcogenides)
- [8] Zeidler et al., “Structure of semiconducting versus fast-ion conducting glasses in the Ag–Ge–Se system,” *R. Soc. open sci.*, vol. 5, no. 1, p. 171401, Jan. 2018, doi: 10.1098/rsos.171401.
- [9] M. Mitkova, Y. Sakaguchi, D. Tenne, S. K. Bhagat, and T. L. Alford, “Structural details of Ge-rich and silver-doped chalcogenide glasses for nanoionic nonvolatile memory: Structural details of Ge-rich and Ag-doped chalcogenide glasses,” *Physics and Statistical Solutions (a)*, vol. 207, no. 3, pp. 621–626, Mar. 2010, doi: 10.1002/pssa.200982902.
- [10] Ricks, “Optical Characterization of Silver-Doped Germanium-Chalcogenide Thin Films,” Undergraduate thesis, Arizona State University, May 2018.

- [11] K. Tanaka and K. Shimakawa, *Amorphous chalcogenide semiconductors and related materials*. New York, NY: Springer, 2011.
- [12] J. M. Conde Garrido, A. Piarristeguy, M. A. Ureña, M. Fontana, B. Arcondo, and A. Pradel, “Compositional dependence of the optical properties on amorphous $\text{Ag}_x(\text{Ge}_{0.25}\text{Se}_{0.75})_{100-x}$ thin films,” *Journal of Non-Crystalline Solids*, vol. 377, pp. 186–190, Oct. 2013.
- [13] M. Mitkova and M. N. Kozicki, “Ag-photodoping in Ge-chalcogenide amorphous thin films—Reaction products and their characterization,” *Journal of Physics and Chemistry of Solids*, vol. 68, no. 5–6, pp. 866–872, May 2007, doi: 10.1016/j.jpcs.2007.01.004.
- [14] X. Zhang et al., “Thermoelectric properties of GeSe,” *Journal of Materiomics*, vol. 2, no. 4, pp. 331–337, Dec. 2016, doi: 10.1016/j.jmat.2016.09.001.
- [15] M. N. Kozicki, M. Park, and M. Mitkova, “Nanoscale Memory Elements Based on Solid-State Electrolytes,” *IEEE Trans. Nanotechnology*, vol. 4, no. 3, pp. 331–338, May 2005, doi: 10.1109/TNANO.2005.846936.
- [16] Y. Yang et al., “Electrochemical dynamics of nanoscale metallic inclusions in dielectrics,” *Nature Communications*, vol. 5, no. 1, p. 4232, Sep. 2014, doi: 10.1038/ncomms5232.
- [17] Y. Yang, P. Gao, S. Gaba, T. Chang, X. Pan, and W. Lu, “Observation of conducting filament growth in nanoscale resistive memories,” *Nature Communications*, vol. 3, no. 1, p. 732, Jan. 2012, doi: 10.1038/ncomms1737.
- [18] D. S. Jayakrishnan, “Electrodeposition: the versatile technique for nanomaterials,” *Corrosion Protection and Control Using Nanomaterials*, Elsevier, 2012, pp. 86–125.
- [19] B. J. Brownlee et al., “Additive manufacturing and characterization of AgI and AgI–Al₂O₃ composite electrolytes for resistive switching devices,” *Journal of Applied Physics*, vol. 128, no. 3, p. 035103, Jul. 2020, doi: 10.1063/5.0004120.
- [20] D. A. Neamen and D. Biswas, *Semiconductor Physics and Devices*, 4th ed. New York, NY: McGraw-Hill, 2007
- [21] “How to calculate the optical band gap from the tauc plot i.e Energy bandgap vs $(\alpha \cdot hv)^2$,” ResearchGate. [Online]. Available: https://www.researchgate.net/post/How_to_calculate_the_optical_band_gap_from_the_tauc_plot_ie_Energy_bandgap_vs_alpha_hv2
- [22] Q. Jin, “Absorption coefficient measurements in the wavelength range 1.3 to 1.6 microns in Bridgman-grown CuInSe₂ with added sodium.” McGill University, 2013.

- [23] J. Tauc, "Optical properties and electronic structure of amorphous Ge and Si," *Mater. Res. Bull.*, vol. 3, no. 1, pp. 37–46, Jan. 1968.
- [24] S. Hassanien and A. A. Akl, "Effect of Se addition on optical and electrical properties of chalcogenide CdSSe thin films," *Superlattices Microstructures.*, vol. 89, pp. 153–169, Jan. 2016.
- [25] J. M. Essick and R. T. Mather, "Characterization of a bulk semiconductor's band gap via a near-absorption edge optical transmission experiment," *American Journal of Physics*, vol. 61, no. 7, pp. 646–649, Jul. 1993, doi: 10.1119/1.17173.
- [26] "Can we calculate Band Gap using tauc plot having y axis (ahv) as the log scale?" *ResearchGate*. [Online]. Available: https://www.researchgate.net/post/How_to_calculate_the_optical_band_gap_from_the_tauc_plot_ie_Energy_bandgap_vs_alphahv2
- [27] K.-H. Song, S.-W. Kim, J.-H. Seo, and H.-Y. Lee, "Characteristics of amorphous Ag_{0.1}(Ge₂Sb₂Te₅)_{0.9} thin film and its ultrafast crystallization," *Journal of Applied Physics*, vol. 104, no. 10, p. 103516, Nov. 2008.
- [28] S. Kumar, D. Singh, and R. Thangaraj, "Electronic structure and optical band gap of silver photo-diffused Ge₂Sb₂Te₅ thin film," *Appl. Surf. Sci.*, vol. 273, pp. 437–443, May 2013.
- [29] Shailendra Kumar Gaur, R. S. Mishra, "Thermal Evaporation and microstructure study of CdTe," *International Journal of Advance Research and Innovation*, vol. 3, no. 2, p. 6, 2015.
- [30] D. K. Schroder, *Semiconductor material and device characterization*, 3rd ed. Piscataway, NJ: IEEE Press, 2006.
- [31] Department of Energy Physics. "Study of semiconductors by UV-Vis spectroscopy." Belarusian State University, 2012. [Online]. Available: http://www.physics.bsu.by/sites/default/files/files/departments/Energy/TEMPUS/CMM_lab/Characterization%20of%20modern%20materials%20-%20Study%20of%20semiconductors%20by%20UV-Vis%20spectroscopy%20-%20TEMPUS%20%28english%20version%29.pdf
- [32] "Optical Profilometry (OP) - nanoAnalytics EN." [Online]. Available: <https://www.nanoanalytics.com/en/services/techniques/optical-profilometry-op.html#Details>
- [33] "Polarized Light Microscopy," Nikon's MicroscopyU. [Online]. Available: <https://www.microscopyu.com/techniques/polarized-light/polarized-light-microscopy>

- [34] K. A. Aly, A. Dahshan, and I. S. Yahia, "Optical constants for Ge_{30-x}Se₇₀Ag_x ($0 \leq x \leq 30$ at%) thin films based only on their reflectance spectra," *Philosophical Magazine*, vol. 92, no. 8, pp. 912–924, Mar. 2012, doi: 10.1080/14786435.2011.637978.
- [35] R. Mishra, "The Temperature Ratings of Electronic Parts", 02-Jul-2019. [Online]. Available: <https://www.electronics-cooling.com/2004/02/the-temperature-ratings-of-electronic-parts/>.
- [36] "Aerospace & Defense Semiconductors: Maxim Integrated," Aerospace & Defense Semiconductors. [Online]. Available: <https://www.maximintegrated.com/en/applications/aerospace-defense.html>.
- [37] "DIY Satellite Platforms," LEO Temperatures. [Online]. Available: <https://www.oreilly.com/library/view/diy-satellite-platforms/9781449312756/ch01s05.html#:~:text=The%20range%20of%20%E2%80%9340%C2%B0,satellite%20electronics%20may%20have%20trouble.>

APPENDIX A

GLOSSARY OF LATERAL PMC DEVICE MICROGRAPHS

Table 1A: Micrographs of 60nm Ge₃₀Se₇₀ + 10nm Ag lateral PMC devices under different bias and temperature, organized by electrode shape

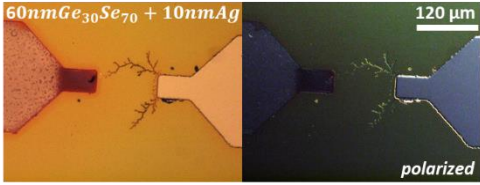
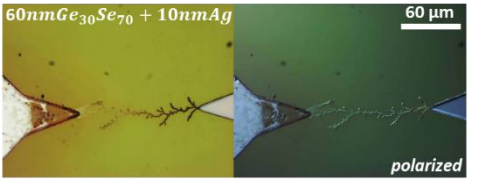
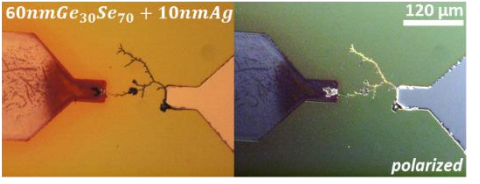
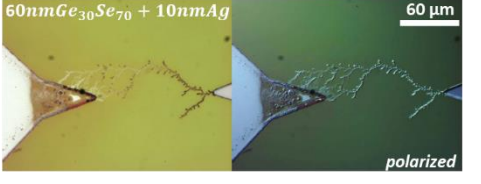
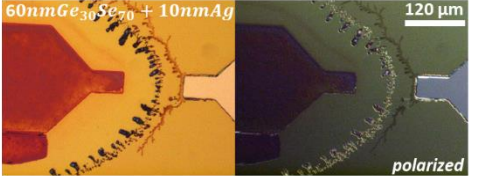
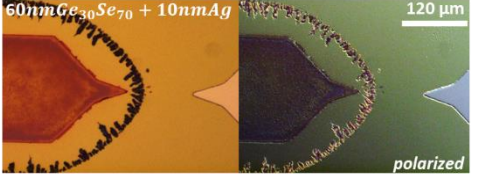
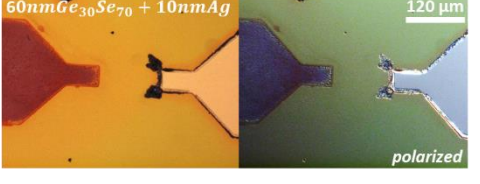
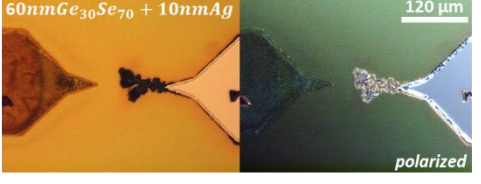
60nm Ge₃₀Se₇₀ + 10nm Ag			
		Square	Sharp
2V	20°C		
	95°C		
1V	20°C		
	95°C		

Table 2A: Micrographs of 60nm Ge₃₀Se₇₀ + 20nm Ag lateral PMC devices under different bias and temperature, organized by electrode shape

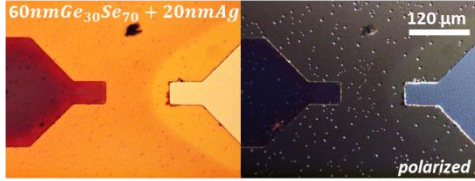
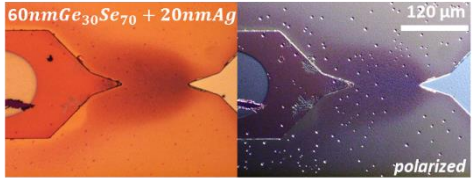
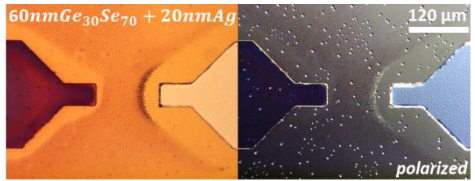
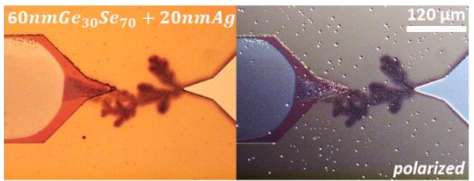
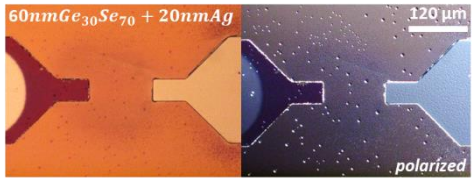
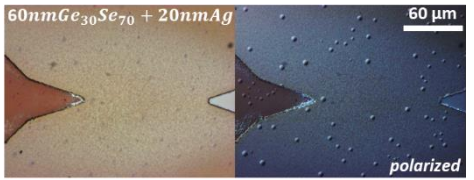
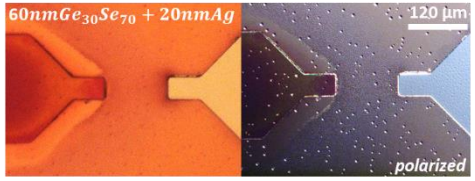
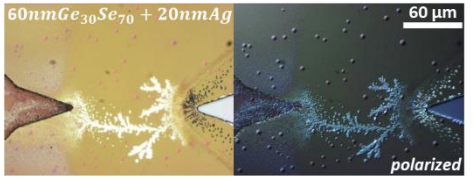
60nm Ge₃₀Se₇₀ + 20nm Ag			
		Square	Sharp
2V	T1		
	T6		
1V	T1		
	T6		

Table 3A: Micrographs of 60nm Ge₃₀S₇₀ + 10nm Ag lateral PMC devices under different temperature, organized by electrode shape

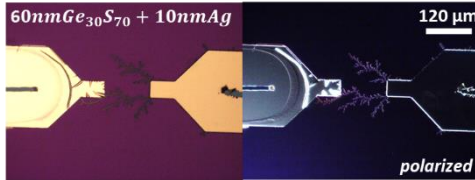
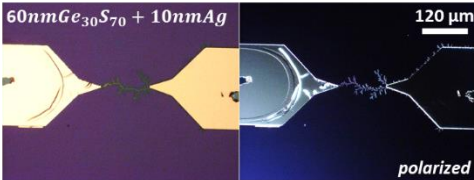
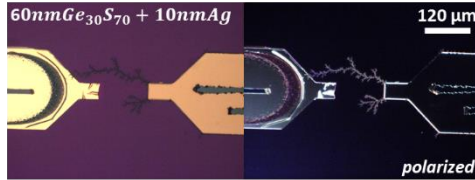
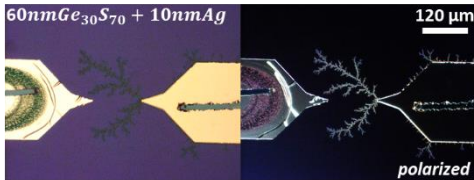
60nm Ge₃₀S₇₀ + 10nm Ag			
		Square	Sharp
2V	T1		
	T6		

Table 4A: Micrographs of 60nm Ge₃₀Se₇₀ + 10nm Ag lateral PMC devices at room temperature, before and after heating to 95°C for 30 minutes, organized by electrode shape

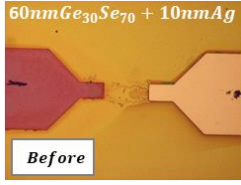
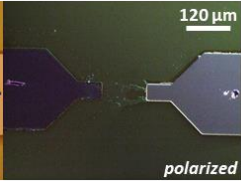
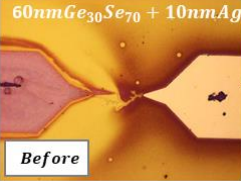
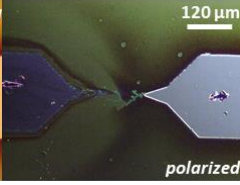
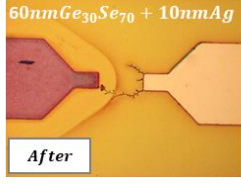
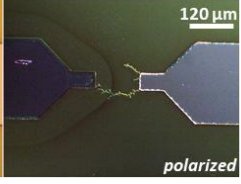
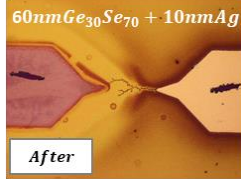
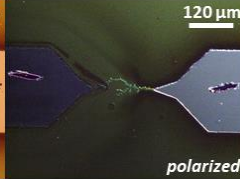
60nm Ge₃₀Se₇₀ + 10nm Ag			
	Square	Sharp	
Before Heating	 	 	
After Heating	 	 	

Table 5A: Micrographs of 60nm Ge₃₀Se₇₀ + 20nm Ag lateral PMC devices at room temperature, before and after heating to 95°C for 30 minutes, organized by electrode shape

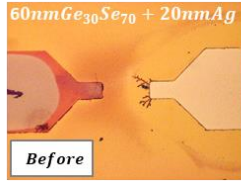
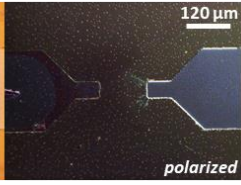
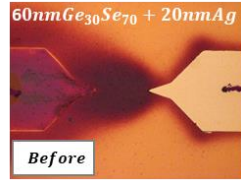
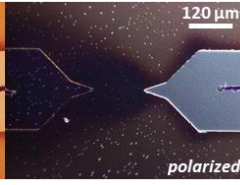
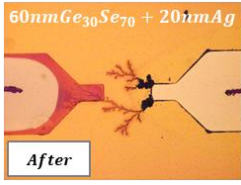
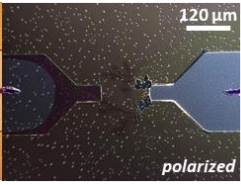
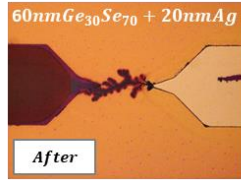
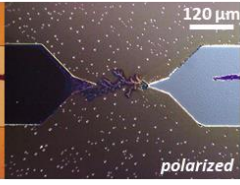
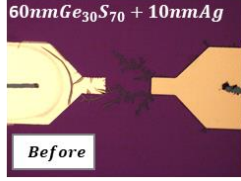
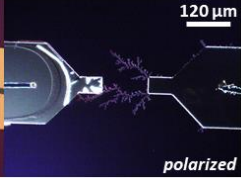
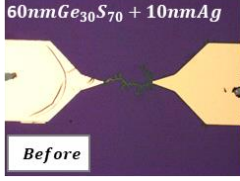
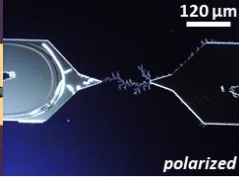
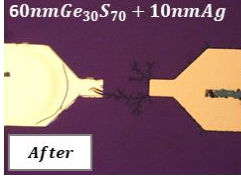
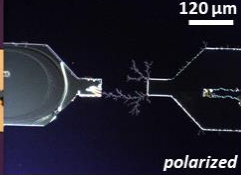
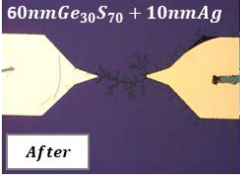
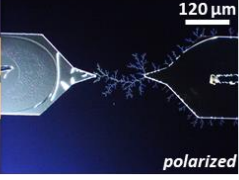
60nm Ge₃₀Se₇₀ + 20nm Ag			
	Square	Sharp	
Before Heating	 	 	
After Heating	 	 	

Table 6A: Micrographs of 60nm Ge₃₀S₇₀ + 10nm Ag lateral PMC devices at room temperature, before and after heating to 95°C for 30 minutes, organized by electrode shape

60nm Ge₃₀S₇₀ + 10nm Ag				
	Square		Sharp	
Before Heating				
After Heating				

APPENDIX B

MEASURED THICKNESS VALUES OF DEPOSITED THIN FILMS

Table 1B: Thickness values for thin films used in Tauc analysis measured using contact stylus profilometry

Chalcogenide	Doping	Photodoping	Radiation	Heating	Thickness (nm)
60nm $Ge_{30}Se_{70}$	-	-	-	-	62.3
60nm $Ge_{30}Se_{70}$	10nm Ag	-	-	-	57.3
60nm $Ge_{30}Se_{70}$	20nm Ag	-	-	-	43.3
60nm $Ge_{30}Se_{70}$	30nm Ag	30 mins	-	-	73.0
60nm $Ge_{30}Se_{70}$	30nm Ag	30 mins	1Mrad	-	70.0*
60nm $Ge_{30}Se_{70}$	30nm Ag	30 mins	-	85°C	70.0*
200nm $Ge_{30}Se_{70}$	-	-	-	-	175.5
200nm $Ge_{30}Se_{70}$	20nm Ag	-	-	-	131.4
60nm $Ge_{30}S_{70}$	-	-	-	-	76.0
60nm $Ge_{30}S_{70}$	10nm Ag	-	-	-	78.9
60nm $Ge_{30}S_{70}$	20nm Ag	-	-	-	93.6
60nm $Ge_{30}S_{70}$	30nm Ag	-	-	-	87.5
60nm $Ge_{40}S_{60}$	-	-	-	-	53.4
60nm $Ge_{40}S_{60}$	30nm Ag	-	-	-	70.0*
60nm $Ge_{40}S_{60}$	30nm Ag	30 mins	-	-	70.0*
60nm $Ge_{40}S_{60}$	30nm Ag	30 mins	100krad	-	70.0*
60nm $Ge_{40}S_{60}$	30nm Ag	30 mins	300krad	-	70.0*
60nm $Ge_{40}S_{60}$	30nm Ag	30 mins	600krad	-	70.0*
60nm $Ge_{40}S_{60}$	30nm Ag	30 mins	1Mrad	-	70.0*
60nm $Ge_{40}S_{60}$	30nm Ag	30 mins	-	450°C	70.0*

*these composition thicknesses were not measured, this estimated value is used in calculations